UNIVERSIDADE DE LISBOA
FACULDADE DE CIÊNCIAS
DEPARTAMENTO DE FÍSICA

Study of the response of plastic scintillators to low energy protons

Duarte Rafael Moreira Guerreiro

Mestrado Integrado em Engenharia Biomédica e Biofísica
Perfil em Engenharia Clínica e Instrumentação Médica

Dissertação orientada por:
Luís Filipe dos Santos Garcia Peralta
João Gentil Mendes Saraiva

2019

ACKNOWLEDGEMENTS

Contei com a ajuda e apoio de várias pessoas não só durante a duração deste trabalho mas também durante todo o meu percurso académico. Quero aproveitar para lhes agredecer.

Em primeiro lugar quero agradecer ao Professor Luís Peralta e ao Dr. João Gentil por supervisionarem este trabalho. Quero agradecer pela ajuda, tempo e conhecimentos que me transmitiram.

Devo um obrigado a todas as pessoas que contribuiram para a realização deste trabalho colocando os seus conhecimentos e arte à minha disponibilidade: Professor Daniel Galaviz, Pamela Teubig, Luís Gurriana, Professor Jorge Sampaio. Quero agradecer ao Campus Tecnológico e Nuclear, na pessoa do Dr. Luís Alves e às oficinas do LIP em Coimbra, na pessoa do Eng. Rui Alves e do Dr. Alberto Blanco.

Um obrigado ao LIP por me dar as condições necessárias à realização deste trabalho.

Quero agradecer aos meus colegas de laboratório pela companhia, conselhos e ajuda: Yoenls Bahu, José Venâncio, Joaquim Kessongo e Ana Campos.

Aos meus amigos pela amizade, ajuda e apoio durante todo o meu percurso académico, um grande obrigado: Rafael Ramos, Francisco Cerdeira, Silvestre Piedade, Filipa Silva, Diana Sousa, João Martins e Luís Araújo.

Obrigado à minha mãe Edite e ao meu pai Carlos por sempre apostarem em mim, mas mais que isso pelos valores que me transmitiram, ao meu irmão Tiago pela sua grande amizade e alegria, aos meus avós pela dedicação e pela sua experiência.

Quero deixar um obrigado especial ao meu avô Álvaro, a quem a vida não permitiu estar comigo até ao fim deste percurso. Quero agradecer pelo carinho que me deu em vida e por continuar a ser um exemplo para mim após a sua partida. Quero dedicar esta dissertação à sua memória.

ABSTRACT

There is real interest in installing in Portugal a proton therapy facility. Proton therapy has a the potential to spare healthy from unnecessary dose. This technology takes advantage of the existance of the Bragg Peak to be able to obtain a dose distribution closer to what is ideal.

Nowadays, ionization chambers are considered the reference in dosimetry. Nevertheless, they offer a poor spatial resolution. Optical fibers, on the other hand, offer a good spatial resolution: with an optical fiber it is possible to achieve a spatial resolution of 2 mm, 1 mm, 0.5 mm or even 0.25 mm. When an optical fiber is irradiated with ionizing radiation it absorbs it and produces scintillation light that is then conducted inside the fiber to a photomultiplier that converts the light in an electrical current.

This work's objective was to develop an experimental setup to study how different optical fibers responds to proton beams, in particular to low energy proton beams. So, this work can be divided in four different stages: development of a software to simulate the interactions of a low energy proton beam with matter; the design and manufacture of a irradiation chamber to block the room light and to make sure that all th light that reachs the photomultiplier is scintillation light; rehabiliation of a X & XY positioning system to be able to place the optical fiber, and irradiation box, with precision; and finally to perform the measurements in the CTN's Van de Graaff.

During the measurements there was made a longitudinal measurement and also a lateral measurement of the beam's profiles. The lateral measurements were performed to better understand the beam's geometry and to obtain the points with a higher signal.

The measurements of the longitudinal profile didn't show the beam's Bragg Peak. This happened for two reasons: first because the beam's energy is too low and all of the proton's energy is deposited in the optical fiber and second because the beam's dispersion means that the number of protons that interact with the optical fiber takes a big fall when the distance is increased.

The lateral measurements were able to confirm that the beam used had a gaussian geometry and enabled the calculation of the security distance from the opening of the irradiation box to the Van de Graff's exit.

Although this setup allowed for the measurements to be made. It still needs some improvements: the positioning system needs motors with a bigger torque and the irradiation box needs to be designed in a more user friendly way. The measurements should be done with a more stable proton accelerator.

Key words: Proton therapy; Scintillator; Optical Fiber; Vand de Graaff.

RESUMO

A terapia com protões é utilizada há vários anos como uma alternativa à mais convencional terapia com raios-X. Durante anos foi vista como aplicável apenas a casos de cancro na base do crânio, para tratamentos feitos em pediatria e para retinoblastomas. Hoje, sabe-se que esta tecnologia pode ser utilizada em todo o tipo de cancros em que a terapia com fotões é utilizada. Em Portugal existe um grande interesse em instalar uma infraestrutura que permita fazer terapia com protões para tratar pacientes oncológicos.A terapia com protões é uma tecnologia que aproveita a existência do pico de Bragg para poupar, até um certo ponto, os tecidos saudáveis a dose desnecessária. Para conseguir isto é necessário ser capaz de mapear com uma pequena resolução espacial o pico de Bragg para os feixes de protões utilizados.

Enquanto que, hoje em dia, as câmaras de ionização são consideradas a referência em dosimetria, estas não oferecem uma pequena resolução espacial. As fibras ópticas, por outro lado, oferecem resoluções espaciais pequenas: 2 mm, 1 mm, 0,5 mm, 0,25 mm. Quando se utiliza uma fibra óptica cintilante para se medir o perfil de dose de um feixe, a fibra é irradiada produzindo luz de cintilação. A luz de cintilação é transmitida dentro da fibra óptica até um fotomultiplicador que converte a luz de cintilação numa corrente eléctrica. O fotomultiplicador é alimentado por uma fonte de alta tensão (o fotomultiplicador utilizado neste trabalho funciona entre os 600 V e os 800 V). A corrente gerada no fotomultiplicador é, finalmente, integrada num electrómetro.

A intensidade da luz de cintilação é, em princípio, linear em relação à quantidade de dose absorvida pela fibra. Contudo, devido a fenómenos de quenching a linearidade é perdida quando a fibra interage com partículas com pouco energia, o que corresponde a um grande stopping power. Esta situação é de especial importância pois é na zona do pico de Bragg que os protões atingem os valores mais elevados de stopping power.

O objectivo deste trabalho foi estudar as características de fibras ópticas cintilantes, em particular as suas respostas a feixes de protões de baixa energia. Para alcançar este objectivo o trabalho foi dividido em quatro partes distintas: desenvolvimento de um software de simulação da interacção de um feixe de protões com a matéria que permitisse a realização de simulações com energia de feixe até aos 15 MeV; uma vez que os protões utilizados têm pouca energia o que levou a que o ar fosse escolhido como fantoma, foi necessário o design e manufacturação de uma caixa de irradiação que permitisse a interacção do feixe de protões com a fibra óptica e que, ao mesmo tempo, impedisse que a luz ambiente interaja com a fibra óptica; montagem de uma mesa XY para conseguir uma colocação precisa da fibra óptica; realização das medições no acelerador de protões do Campus Tecnológico e Nuclear.

Quando se pretende fazer leituras de dose com fibras ópticas não se pode permitir que a luz ambiente interaja com a fibra óptica pois isso altera os valores medidos pela electrónica. No caso das medições de dose com fotões é possível utilizar-se uma manga para impedir esta interacção. No caso de um feixe de protões tal não é possível pois isso altera a energia do feixe de protões antes de estes interagirem com a fibra óptica. A solução encontrada foi desenhar uma caixa de irradiação onde a fibra é introduzida durante as medições. Esta caixa de irradiação tem uma abertura por onde entra o feixe de protões, esta abertura é coberta com uma fina janela de prata (a janela de prata utilizada nas medições tem 210 nm de espessura). A espessura das janelas de prata foi medida usando a perda de energia de partículas alfa no material da janela.

A necessidade de ter uma colocação precisa da fibra óptica foi sentida deste o ínicio, pois sem uma colocação precisa a boa resolução espacial oferecida pela fibra óptica seria inútil pois existiria uma grande incerteza no ponto do espaço em que a fibra é colocada. O sistema de posicionamente escolhido foi uma mesa XY.

As simulações realizadas com o pMC foram feitas tendo em conta um volume de fibra semelhante nao volume de fibra que é irradiado nas medições experimentais, uma janela de prata de espessura igual à espessura da janela utilizada nas medições experimentais e considerando que o fantoma é composto por ar. Este novo software foi comparado com o software de simulação FLUKA que também foi utilizado nas simulações utilizadas neste trabalho.

Durante as medições foi feita uma medição do perfil longitudinal do feixe e foi também feita uma medição do perfil lateral do feixe. A leitura do perfil lateral do feixe foi feita para conseguir entender melhor a geometria do feixe e para conseguir obter os pontos com um maior sinal para se considerar esse ponto para o perfil longitudinal usando a leitura de sinal na fibra óptica colocada em várias posições.

As simulações mostraram que existem algumas diferenças entre o pMC e o FLUKA. Estas diferenças podem ser explicadas com o facto de as bases de dados dos stopping power utilizadas no pMC e no FLUKA são diferentes e com o facto de o algoritmo de dispersão ter uma componente lateral menor no pMC.

As medições laterais permitiram demonstrar que o feixe possui uma geometria gaussiana e permitiram calcular a distância de segurança (distância entre a caixa de irradiação e a saída do feixe, necessária para não perfurar a janela de prata) a que a caixa é colocada da saída do acelerador.

As medições do perfil longitudinal do feixe não permitiram que o pico de Bragg do feixe fosse observado. Isto acontece por várias razões: primeiro porque a energia do feixe é pequena e dos protões não conseguem atravessar a fibra o que faz com que o que é lido seja a energia do protão em vez de a energia deixada pelo protão num determinado volume; segundo porque a dispersão do feixe faz com que o número de protões que interagem com a fibra óptica baixa com a distância e isso baixa bastante a quantidade de energia absorvida pela fibra óptica; a distância entre duas posições consecutivas da fibra é demasiado grande para se poder considerar que temos uma variação pequena de energia. As simulações em que uma geometria gaussiana e uma desalinhamento da fibra óptica em relação à saída do feixe é considerada são as que mais se aproximam das medições experimentais.

Como conclusão podemos dizer que apesar de ter sido possível realizar uma série de medições com este dispositivo experimental ainda é necessário realizar alterações ao mesmo. A caixa de irradiação deve ser mais fácil de utilizar, principalmente no que toca à introdução das fibras. O sistema de posicionamento precisa de ser melhorado pois os motores não oferecem torque suficiente para fazer com que percorra toda a distância da calha. É necessário utilizar outro feixe de protões pois o Van de Graaff utilizado no CTN apresenta muitas oscilações na intensidade do feixe.

PALAVRAS CHAVE: Terapia com protões; Cintilador; Fibra Óptica; Van de Graaff.

CONTENTS

LIST OF FIGURES

LIST OF TABLES

LIST OF ABBREVIATIONS

IRCU International Comission on Radiation Units & Measurements

LET Linear Energy Transfer

PS Polysterene

MC Monte Carlo

CTN Campus Tecnológico e Nuclear

POM Polyoxymethylene

POF Plastic Optical Fiber

SOF Silica Optical Fiber

PMMA Polymethyl methacrylate

1 INTRODUCTION

1.1 MOTIVATION

Cancer is one of the deadliest diseases that exist. Therefore, there is a lot of effort put into tackling it. There is real interest in installing in Portugal a proton therapy facility. This facility creates the necessity to perform several studies in proton therapy dosimetry. The reason why proton therapy is so interesting has to do with the existence of the Bragg Peak (the Bragg Peak is the rapid increase in stopping power on the end of a charged particle's trajectory), which allows to spare from damage, to some extent, the healthy organs surrounding the tumor. Therefore, it is of high relevance to study a proton beam's Bragg Peak. This work's objective to study the behaviour of materials to proton energy deposition around the Bragg Peak for a certain proton beam energy using scintillating optical fibers and to study the response of plastic scintillators to proton beams of small to intermediate energy, wich corresponds to energies below 20 MeV. The non-linear response of the scintillator to energy deposition will also be addressed.

1.2 CANCER

Cancer is a group of diseases characterized by an uncontrolled growth and division in a group of cells. It is a genetic disease and is caused by a change in the genes that control the way the cell works and, specially, how it divides. The way cancer can hurt organisms is by: invading or developing in fundamental organs and using the resources that the organs need (oxygen and nutrients), and also by releasing toxins that damage the healthy tissues [7].

Initiation and progression of cancer depends on both external factors (tobacco, chemicals, radiation and infectious organisms) and internal factors (inherited mutations, hormones, immune conditions, and mutations that occur from metabolism) [8]. These factors can work, together or in sequence, resulting in a tumor growth that affects surrounding normal tissues, and can even result in metastasis.

The genes that have an effect in tumor appearance can be divided in oncogenes, these are genes that promote cell growth and reproduction, and tumor suppressor genes that inhibit cell division and survival. The appearance of novel oncogenes, and the over-expression of normal oncogenes or the under-expression of tumor suppressor genes can lead to the appearance of a tumor [8].

Cancer is one of the most deadly diseases that exist:

- Cancer is nowadays the second most deadly disease, second only to cardiovascular diseases. This disease is responsible for a estimate 9.6 million deaths in 2018. This results in 1 in 6 deaths worldwide [9].
- According to the American Cancer Society more than 1.7 million new cancer are expected to be diagnosed in 2019 and about 606.808 Americans are expected to die from cancer in 2019 [10].
- There were an estimate 3.91 million new cases of cancer and 1.93 million deaths from cancer in Europe in 2018 [11].

To treat cancer three main approaches can be used: radiotherapy, chemotherapy and surgery. These three ways can be used together or isolated. Radiotherapy is heavily used for cancer curative or palliative treatment. More than 14 million new cases of cancer are diagnosed globally each year. Radiation therapy has the potential to improve the rates of cure of 3.5 million people and provide palliative relief for an additional 3.5 million people [12].

1.3 RADIOTHERAPY

1.3.1 HOW DOES IT WORK?

Radiotherapy works in two ways,in a **direct way** and in a **indirect way**:

- The **direct way** works by directly ionizing, and in consequence destroying some macro-molecules present in the cell's membrane, cytoplasm and most importantly destroying the tumor cell's DNA molecules. One or more chemical bonds may be broken resulting in atoms or molecules with unpaired electrons. The bonds broken can be repaired but the atoms or molecules can also bond with another free radicals [13]. This type of direct process occurs more often with high Linear Energy Transfer (**LET**) radiation, such as protons.This feature is important because high LET particles can be very effective even in situation of low oxygen supply to the tumor cell [13].
- The **indirect way** works by ionizing water molecules (water radiolysis) what creates free radicals (OH^-, H^+) in the cell's cytoplasm that have high reactivity towards cell's molecules, lipids and DNA.

Another important factor to consider in the usage of radiotherapy is the dissemination of the tumor cells throughout the body. If the tumor cells are widely spread, like a in leukemia or with a highly metastasized cancer the treatment with radiation becomes inefficient. In tumors that are in an early stage and localized, like breast cancer, for example, radiotherapy is highly efficient.

1.3.2 RADIOTHERAPY SIDE EFFECTS

Although radiotherapy is very useful to fight cancer, the usage of radiation can have some serious side effects [14]:

- Fibrosis : the radiation can cause a loss of elasticity on the tissues irradiated .
- Secondary Cancers : radiation is one of the most common causes of cancer. The risk of developing a tumor after irradiation grows as the dose goes up. The area is also important since certain organs, such as the breast and thyroid, seem to be more likely to develop cancers after radiation than others.
- Heart disease: Radiation therapy can damage the heart and increase the risk of the patient suffering a a heart attack or stroke. The damage to the heart and the increase in the risk of disease are dose dependent.
- Hampering of cognitive ability: When the tumour is localized near the brain, radiation treatment can make the cognitive abilities decline, specially when the patient is of young age.

Taking into consideration all these side effects it is expected that clinicians look for ways of lowering the dose absorbed by healthy tissues. Through dosimetric techniques it is possible to make dose predictions, using simulations and experimental measurements with phantoms, and to know how to decrease the amount of dose absorbed by the patient.

1.3.3 PROTON THERAPY

The clinical rational to invest and develop a new radiation treatment is the possibility of improving the treatment outcome of the patient, for instance, with a more conformal dose distribution. [15]. An ideal dose distribution is one that is confined to the tumor volume. Although that is not possible to achieve with proton therapy, it represents a clear improvement over photon therapy [15]. The reason for this is the existence of the **Bragg Peak**, shown in Figure 1.1.

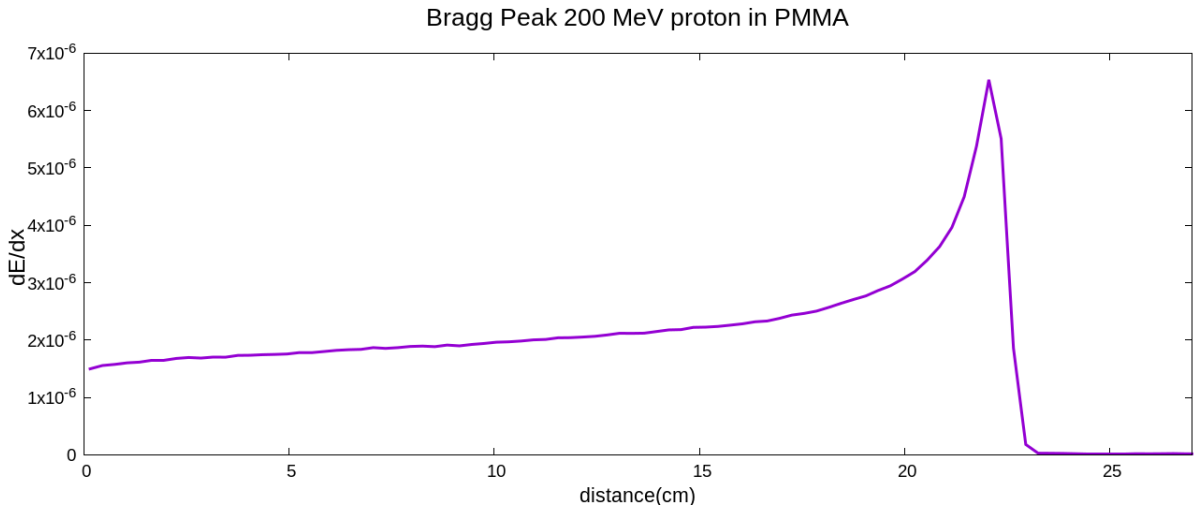

Figure 1.1: Simulation of the interaction between a proton beam and PMMA.Simulations performed with FLUKA.

The existence of the Bragg Peak is of such importance because after it the dose transferred to healthy tissues is negligible, in other words after the steep fall in the graphic the dose is essentially zero and that provides the clinical professionals the possibility to tighten the security boundaries when compared to photon therapy.

1.4 WHY OPTICAL FIBERS?

The currently used standard for dosimetry is the ionization chamber [16], but this type of device offers a poor spatial resolution (between 1 mm and 2 mm) [17]. Moreover, it is important to know with high precision the position of the end of the Bragg Peak, for the reason that,it may enable the reduction of the margins around the tumour volume.

In order to know with precision the position of the Bragg Peak it is desirable to have a spatial resolution smaller than one milimeter. Using plastic optical fibers it is possible to achieve spatial resolutions equal to the fiber's diameter: 2 mm, 1 mm, 500 μm, 250 μm and so a really small spatial resolution can be achieved with optical fiber's.

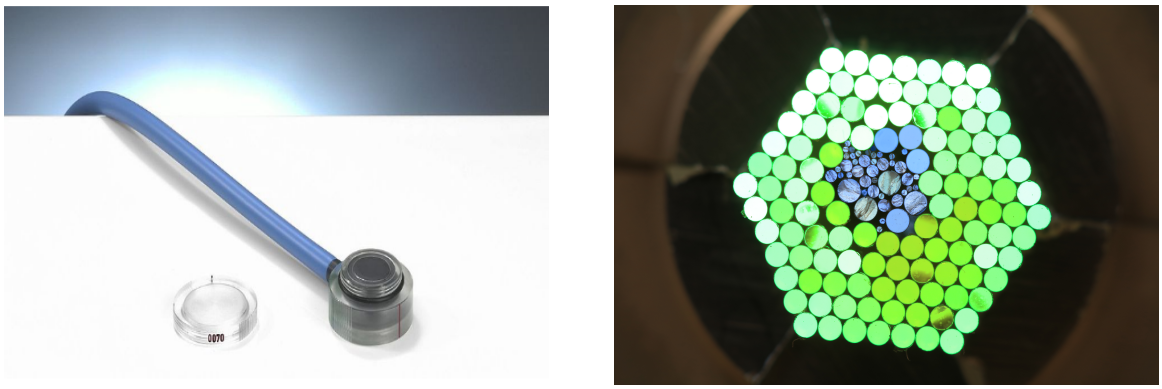

(a) (b)

Figure 1.2: (a) A Markus ionization chamber,(b) a bundle of optical fibers, the blue ones are the scintillating fibers.

1.5 DIFFERENT WORK STAGES

When working on scintillation dosimetry it is important to work on the simulations and to develop a proper setup to perform the experiment. Because of it this work is divided into four different stages:

- Development of a fast software to simulate the interaction of protons with matter, that creates the possibility

to do the kind of simulation needed, because the type of scoring used is completely up to the user and it creates the possibility to do in a faster way a larger number of simulations;

- Design and manufacture of a phantom to be able to perform the measurements in air without disturbing too much the beam and making sure that the optical fiber doesn't interact with room light;
- Rehabilitation of a XY positioning system to perform the measurements with the most accuracy possible;
- Perform the measurements and compare them with the simulations to extract important information.

This work was used in the ICDA3 conference [18] . The experimental results were featured in a presentation a poster was made regarding pMC.

2 METHODS

2.1 INTERACTION OF RADIATION WITH MATTER

Proton therapy and photon therapy differ by the kind of interaction that the particle used has with matter (charged particles and photons, respectively). The International Comission on Radiation Units & Measurements (**IRCU**) recommended the distinction between radiation that directly ionizes matter and radiation that indirectly ionizes matter [19]:

- Directly Ionizing Radiation (fast charged particles): They deposit their energy in matter in a direct way, through a series of Coulomb interactions along the particles path;
- Indirectly Ionizing Radiation (photons and neutrons): this type of radiation first transfers its energy to charged particles present in matter in a small number of interactions (in each one of these interactions they transfer a big portion of their energy). In their turn the fast charged particles that result from this interaction transfer their energy to matter.

Since the subject of this work is proton therapy it will focus from now on Direct Ionizing Radiation.

A charged particle interacts with electrons and the nucleus of the atoms through a Coulomb field. The types of Coulomb interactions between charged particles are:

- **Soft collisions**: when a charged particle passes through an atom at a considerable distance, then the effect of the Coulomb field interaction affects the atom as a whole: distorting it, exciting it or even ionizing it. The total effect is the transfer of a small amount of the kinetic energy of the charged particle to an atom of the absorbing medium. This happens to be the most common way of collision;
- **Hard collisions**: It can happen that the charged particle interacts directly with an atomic electron, transferring to it a considerable amount of kinetic energy which makes the electron leave the atom (ionizing it) and gain the name of delta ray. Delta rays are energetic enough to dissipate their kinetic energy through Coulomb-force interactions, although they do it in a track different from the one travelled by the primary charged particle.

Protons can also interact with matter through Nuclear Interactions, but in the scope of this work high energy interactions won't be considered.

2.1.1 STOPPING POWER

The mean rate of energy loss for moderately relativistic charged heavy particles is given by the Bethe equation:

$$\left\langle -\frac{dE}{dx} \right\rangle = Kz^2 \frac{Z}{A} \frac{1}{\beta^2} \left[\frac{1}{2} ln \frac{2m_e c^2 \beta^2 \gamma^2 W_{max}}{I^2} - \beta^2 - \frac{\delta(\beta\gamma)}{2} \right] \tag{2.1}$$

this equation [20] is valid for $0.1 < \beta_\gamma < 1000$ and for intermediate Z materials. It also represents the mass stopping power where K equal to $4\pi N_A r_e^2 m_e c^2$, z is the charge number of incident particle, Z is the atomic number of the absorber. A is the atomic mass of the absorber, $m_e c^2$ is the electron mass $\times$ c^2, I is the mean excitation energy. $\delta(\beta_\gamma)$ is the density effect correction to ionization energy loss. The mass stopping power units are in MeV g^{-1} cm ^{2}. The linear stopping power is $\left\langle -\frac{dE}{dx} \right\rangle \rho$ where ρ is the density in g/cm^3 and has units MeV/cm.

The expression inside straight brackets in equation 2.1 varies slowly with particle energy. Thus, the general behavior of dE/dx can be inferred from the behavior of the multiplicative factor. For a given nonrelativistic particle, dE/dx varies with β^2, therefore, inversely with the particle's energy. This can be explained visualizing that when a particle spends more time in the vicinity of an electron the impulse felt by the electron is larger, and hence, the energy transfer is also larger. When comparing different particles, in equation 2.1 it is seen because of z^2 that, for

the same velocity, particles with the greatest charge will have a larger dE/dx. For different absorber mediums, dE/dx depends primarily on the product NZ. This product represents the electron density of the absorber. With higher electron densities dE/dx is also higher.

The fact that the expression inside straigh brackets varies inversely with the particle's energy is the reason for the existance of the Bragg Peak. Near the end of the track, the charge is reduced through electron pickup and the curve falls off [21].

Figure 2.1 shows how the stopping power varies as a function of the particle's energy for protons in different materials.

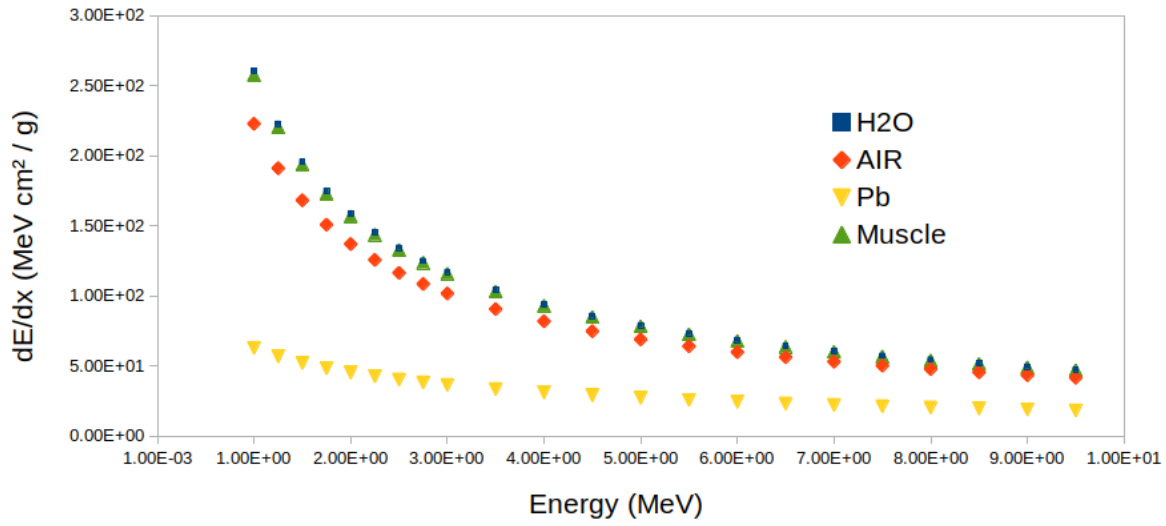

Figure 2.1: Stopping power for protons as a function of the kinetic energy.

2.2 SCINTILLATION

2.2.1 SCINTILLATION PHYSICS

Organic scintillators are aromatic hydrocarbon compounds which contain benzene ring structures interlinked in various ways [22].The fluorescence process in organics arises from transitions in the energy level structure of a single molecule. So the organic scintillators can scintillate in many diferent forms: as a polycristaline material, as a vapor, or as part of a multicomponent solution.

A large category of organic scintillators is based on organic molecules with certain properties that give rise to the π-electron structure. The π-electronic energy levels of such a molecule are illustrated in the figure 2.2. Energy is absorbed by exciting the electron configuration into any one of a number of excited states. The states that have spin equal to zero are labeled as S_0,S_1,... in the same figure. The molecules that can be used as organic scintillators have a gap in energy between level S_0 and S_1 is 3 or 4 eV, and the energy gap between higher-lying states is usually somewhat smaller. Each of these states is subdivided into states that correspond to the vibrational state of the molecule. So, an additional subscript is added to distinguish these vibrational states: the symbol S_{00} represents the vibrational state with the least energy in the ground electronic state.

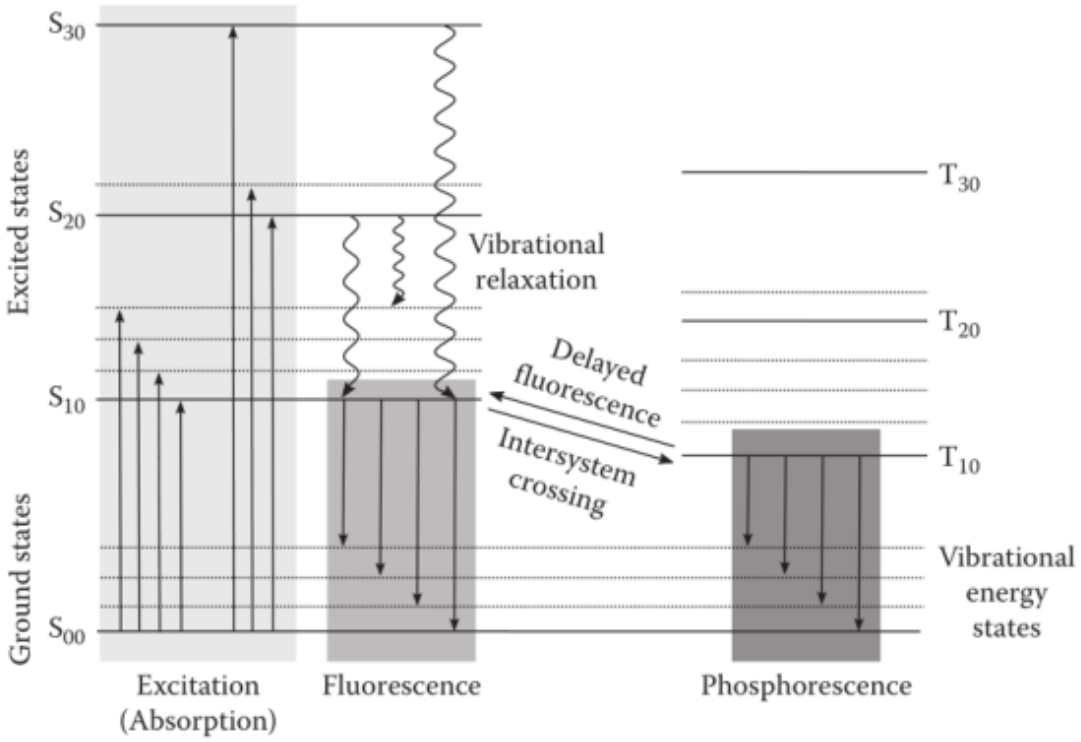

Figure 2.2: Molecular mechanism that leads to the scintillation of organic scintillators [1].

Nearly all molecules, at room temperature, are at the S_{00} state. When a charged particle passes nearby there is an absorption of energy that is represented by the arrows point upward in figure 2.2. The result of this excitation process is a population of excited molecules in the S_{10}. This happens because the excess energy that permits the molecules to go to an higher level is quickly dissipated through radiationless internal convertion.

The scintillation light is emmited in transitions between the S_{10} and the ground electronic state.

2.2.2 SCINTILLATION EFFICIENCY

Several things diminish the signal read: the scintillating material doesn't have an efficiency of one hundred per cent, there is attenuation when the light travels from the spot in the fiber where it is originated to the PMT and the PMT's, generally, have low efficiency (20 %-30 %). All these phenomena explain some of the loss in the signal.

The existence of the quenching phenomena also explains some loss in the signal, more specifically it explains the loss of linear relation between the stopping power of the particle and the signal produced by the optical fiber.

Scintillators cannot convert all the energy transferred to them to visible light, which means there is a portion dissipated in nonradiative ways, as stated above. The portion of original energy transformed into scintillation light can be regarded as the scintillation efficiency. Neglecting the fact that there is quenching happening, the fluorescence energy per unit path lenght, $\left(\frac{dL}{dx}\right)$ can be related to the charged particle energy loss $\left(\frac{dE}{dx}\right)$ that depends on the particle type and energy, with the scintillation efficiency (α):

$$\frac{dL}{dx} = \alpha \frac{dE}{dx} \tag{2.2}$$

2.2.3 QUENCHING

The quenching phenomena represents the loss of efficiency in the conversion of ionizing energy to visibe light. Quenching is problematic for scintillation dosimetry of proton beams, limiting the usefulness of scintillator detectors

for measuring dose distributions. Knowing that the scintillator's response depends on the incident radiation, that is usually quantified as $\frac{dE}{dx}$ and knowing that it varies mainly in depth direction it leads to a depressed signal in the Bragg peak of proton beams, as is seen in figure 2.3.

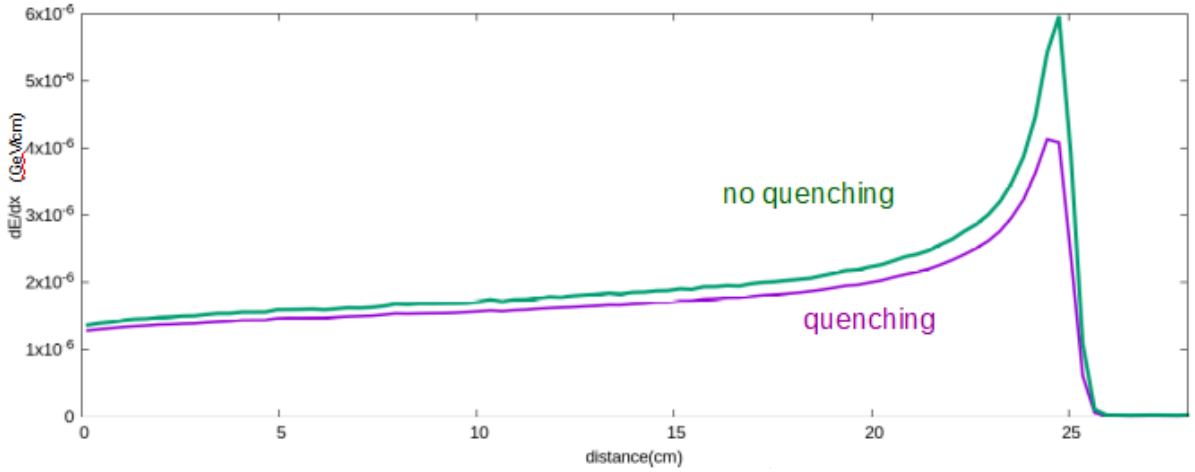

Figure 2.3: Signal read with a PMMA scintillator considering the quenching phenomena in comparison with the signal read without considering the quenching phenomena. The simulation was performed using FLUKA.

2.2.4 PHYSICAL EXPLANATION OF QUENCHING

There are two main proposed explanations for the quenching phenomena:

- The first has to do with the saturation of the scintillation centers. Meaning that if all the scintillation centers in a certain region get excited, due to a high deposition of energy, an increase in the energy depostion will not lead to an increase in the light output. This hypotesis is supported by the fact that quenching phenomena depends on $\frac{dE}{dx}$. Acording to this hypothesis it is expected that increasing the concentration of scintillators centers should decrease the quenching phenomena, however this is not verified [23] [24].
- The second proposes that quenching has to do with a decrease in the efficiency of the primary excitation of the scintillator. In other words, regions of the scintillator with a bigger ionization density become less efficient in transfering the energy from the ionizing radiation to the excited state. One explanation of this mechanism was proposed by Jonh Birks $(1920 - 1979)$. Birks proposed that this decreased in efficiency is a consequence of damage to the scintillator molecules. This leads to the most commonly used quenching model: Birk's Molecular Damage Model.

2.2.5 BIRK'S MOLECULAR DAMAGE MODEL

This model relates the light yield per unit path lenght $\frac{dL}{dx}$ to the differential energy deposition of a charged particle $\frac{dE}{dx}$, using the scintillation efficiency α and the quenching parameter kB.

$$\frac{dL}{dx} = \frac{\alpha \frac{dE}{dx}}{1 + kB\frac{dE}{dx}} \tag{2.3}$$

The term $B\frac{dE}{dx}$ is the specific density of excited and ionized molecules, and the parameter k is the quenching parameter. These two parameters appear together, often, because they are hard to measure separately [1], and are treated as a material-specific quenching parameter kB. It can be added to Birk's model a second-order coefficient:

$$\frac{dL}{dx} = \frac{\alpha \frac{dE}{dx}}{1 + kB\frac{dE}{dx} + C\left(\frac{dE}{dx}\right)^2} \tag{2.4}$$

The parameter C is linked to various processes in the scintillator, one of those being biomolecular quenching, but most important is that it becomes an additional degree of freedom to obtain a better fit to experimental data.

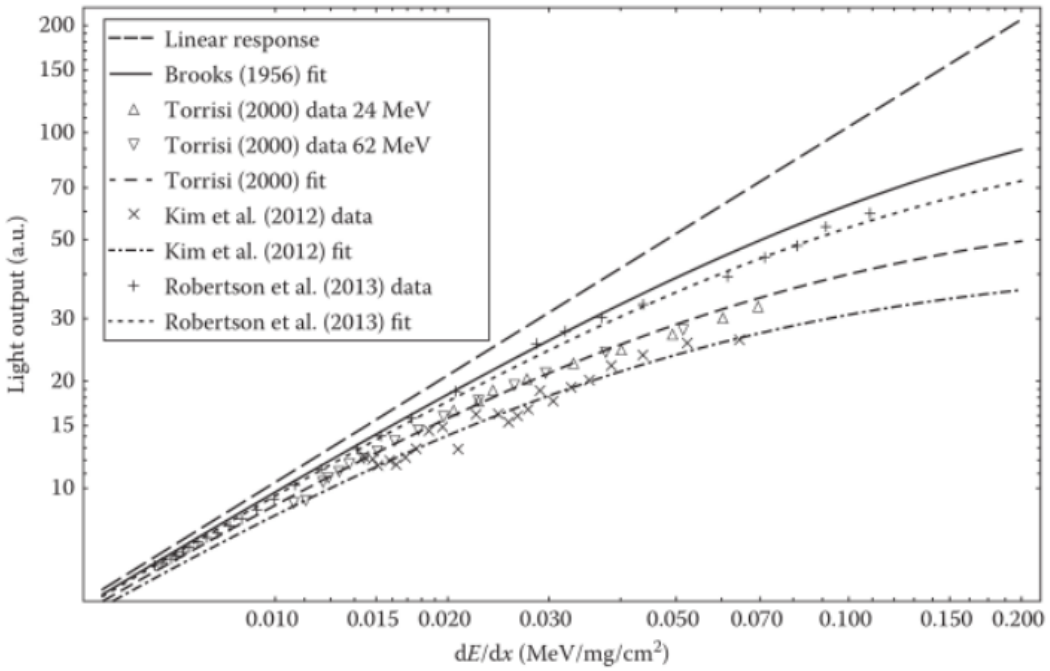

Figure 2.4: The effect of quenching in the response of optical fibers (or other plastic scintillators) when they interact with particles with high dE/dx.It is possible to see that for the higher values of dE/dx the output of the scintillator becomes less linear [1]

When $\frac{dE}{dx}$ tends to infinite the equation 2.3 becomes $\frac{\alpha}{KB}$ wich translates a saturation in the light output. Moreover, in figure 2.4 it is visible that for higher values of $\frac{dE}{dx}$ the energy resolution is worse than the resolution for lower values of $\frac{dE}{dx}$.

2.2.6 DOSIMETRY

The most important variable in dosimetry is, as the name suggests, the dose. The absorbed dose is defined in relation to a stochastic quantity called energy imparted, ϵ. The equation that defines energy imparted by ionizing radiation to matter of mass m in a finite volume V is:

$$\epsilon = (R_{in})_u - (R_{out})_u + (R_{in})_c - (R_{out})_c + \sum Q \tag{2.5}$$

where: $(R_{in})_u$ is the radiant energy of uncharged particles entering V, $\sum Q$ is the net energy derived from the rest mass in V, $(R_{in})_c$ is radiant energy of the charged particles entering V, and $(R_{out})_c$ is the radiant energy of the charged particles leaving V.

The dose D can now be defined at any point P in V as

$$D = \frac{d\epsilon}{dm} \tag{2.6}$$

Thus , the absorbed dose D is the expected value of energy imparted to matter per unit mass at a certain point.

The absorbed dose rate at point P and time t is given by

$$\frac{dD}{dt} = \frac{d}{dt}\left(\frac{d\epsilon}{dm}\right) \tag{2.7}$$

2.3 EXPERIMENTAL SETUP

To use the response of plastic scintillators to a map proton beam is absolutely necessary to have a proton beam source, a plastic scintillator and the readout electronics. And so, the experimental setup consisted of a proton accelerator, a Van de Graaff accelerator, a phantom made of aluminum, a set of optical fibers, a positioning system, a photo-multiplier tube and measurement devices.

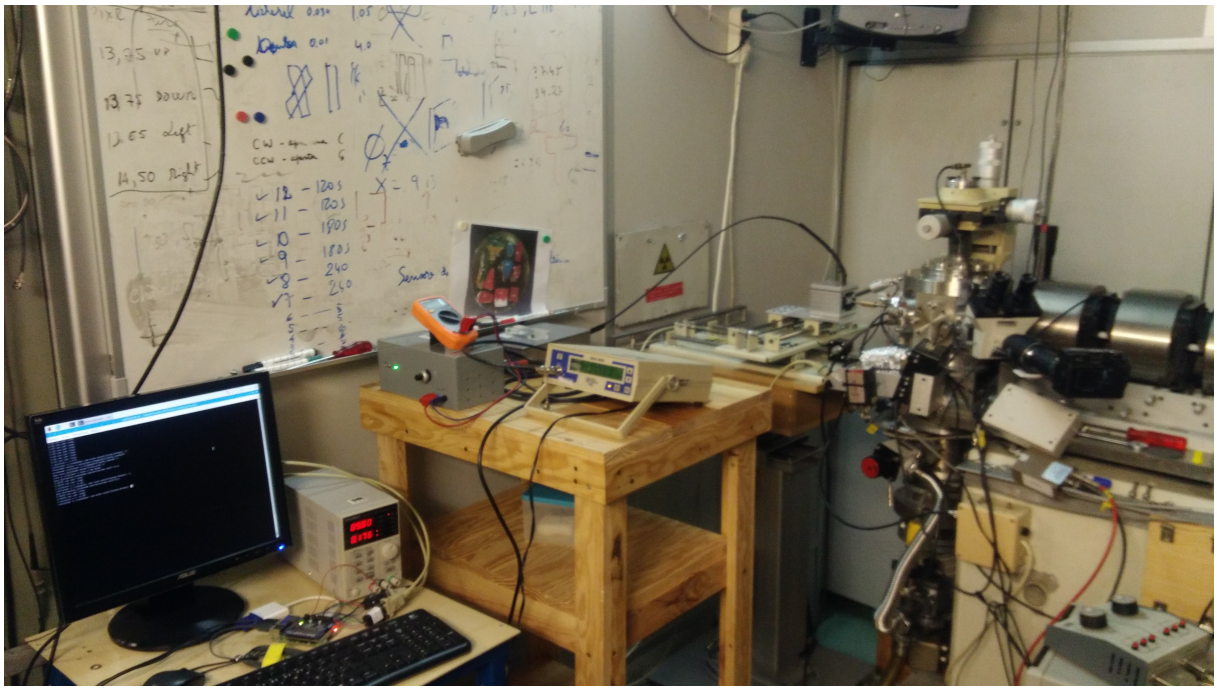

Figure 2.5: The experimental setup for aquisition with the 2 MeV proton beam at CTN. From left to right: the positioning system control station, the readout electronics, the phantom and optical fiber and one of the beam pipe exit coming from the Van de Graaff accelerator.

Air was chosen to be the medium where the dose is measured. This may sound strange, because in normal conditions the medium should be something with it's characteristics closer to those of the human body, like PMMA, for example. Nevertheless, it is important to remember that in portuguese territory there is no technology that can produce a proton beam with the energy levels used in radiotherapy (200-250 MeV), and besides that the proton accelerator that was available during the time this thesis was made only produces a proton beam with 2 MeV. Because of that and due to the fact that a 2 MeV proton beam has a very low range in PMMA (70 μm), according to NIST, the chosen media was air so that the proton can travel a much greater distance (7 cm) [2].

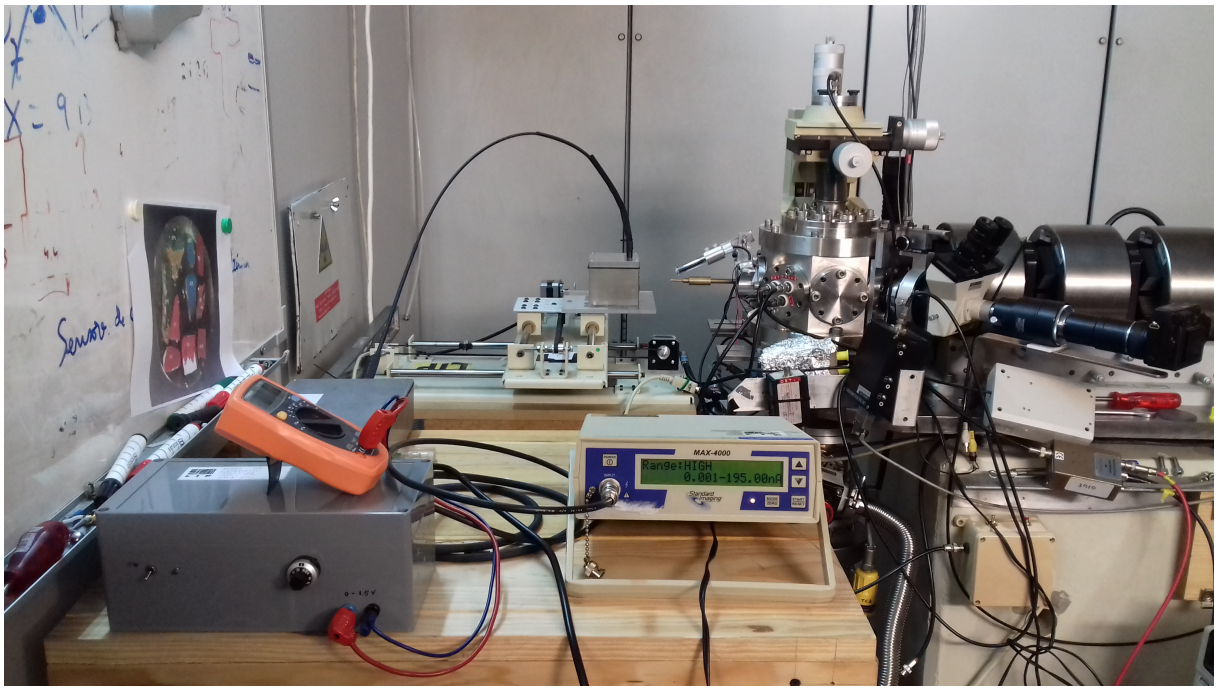

Figure 2.6: The experimental setup for aquisition with the 2 MeV proton beam at CTN. In the front the HV source and the electrometer are seen and in the back is seen the positionin system, the irradiation box and the beam pipe exit coming from the Van de Graaff accelerator.

The 2 MeV beam can be used to study the response of a system that is designed to study a radiotherapy beam because the most important part of the beam is the Bragg Peak and it is important to remember that in the Bragg Peak zone the beam's energy is lower than the initial beam's energy.

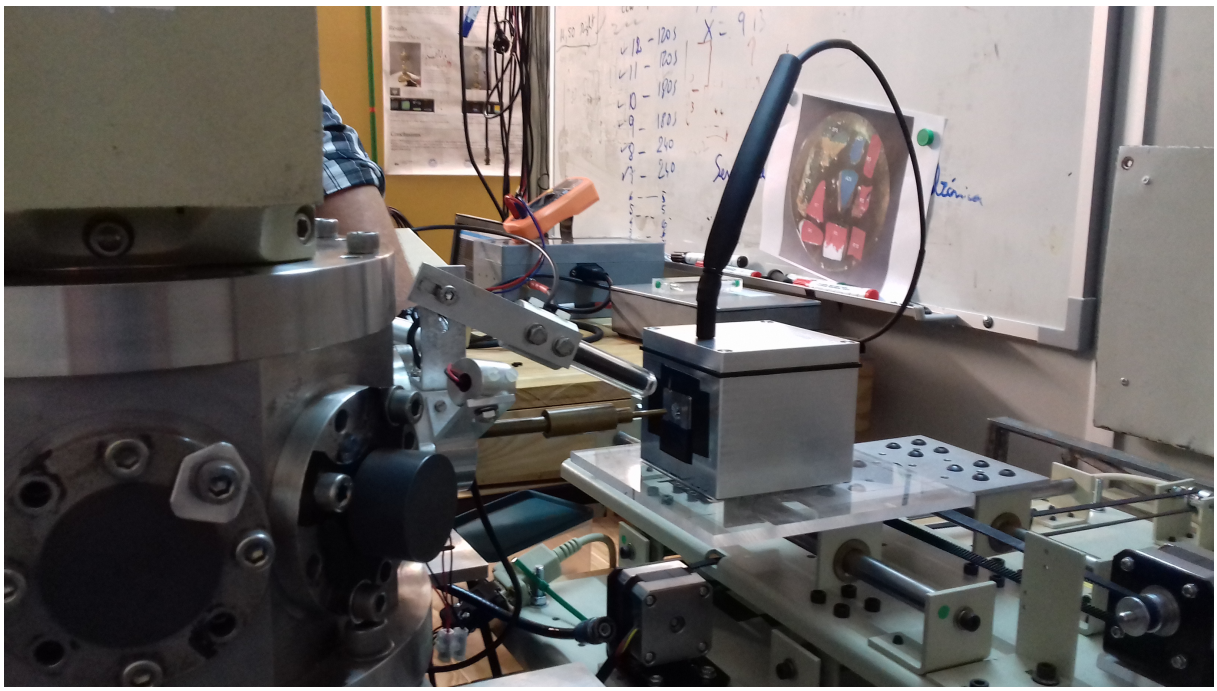

Figure 2.7: The experimental setup for aquisition with the 2 MeV proton beam at CTN. The exit of the pipe is close to the silver window the optical fiber is also seen inserted in the irradiation box.

2.4 EXPERIMENTAL SETUP CONCEPT

When using scintillators to measure energy deposition the main idea is that when scintillators are irradiated with ionizing radiation they absorb it and emit the absorbed energy in the form of light. The light is then read, using a photomultiplier and an electrometer as is seen in figure 2.8. The electric signal generated is, in principle, proportional to the absorbed dose.

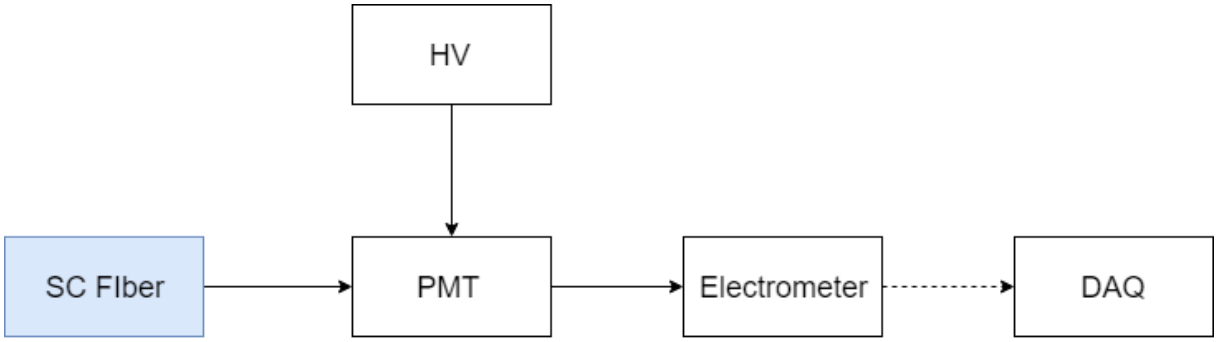

Figure 2.8: Block Diagram that represents the generic setup necessary in scintillation dosimetry.In this figure HV stands for High Voltage, SC Fiber stands for Scintillating Fiber, PMT stands for Photomultiplier Tube and DAQ stands for Data Acquisition.

2.5 OPTICAL FIBERS

As a dielectric waveguide, an optical fiber can transmit light signals from a light source to a light-measuring device by total internal reflection. With Snell's Law it is possible to extract the condition that leads to total internal reflection:

$$n_1 sin(\theta_1) = n_2 sin(\theta_2) \tag{2.8}$$

So that a ray of light to be internally reflected it must be incident on a boundary from a medium with a higher refractive index to another with a lower refractive index. If a ray of light transmits with a certain incident angle (θ_1) that is less than the critical angle (θ_c) from a medium 1 with a refractive index (n_1) to medium 2 with a low refractive index (n_2), a portion of light will be reflected back to medium 1 with a reflection angle (θ_1) and another portion of light will be refracted into medium 2 with a refraction angle (θ_2).

When the incidence angle (θ_1) is increased to the critical angle (θ_c), the refractive angle (θ_2) reaches 90^o, and thereby, a ray of light travel along the interface region between two contacted media. Here, the critical angle (θ_c) is defined as:

$$\theta_c = sin^{-1}\left(\frac{n_2}{n_1}\right) \tag{2.9}$$

Above the critical angle the total internal reflection is reached.

Nearly all commercial optical fibers are classified into plastic optical fibers (POF) and silica optical fibers (SOF) according to the core constituent material. As a light, for medical uses, POF's have many advantages over commercially available SOF's, including low cost, ease of use, light weight, large core diameter, and good flexibility.

In general, polymethyl methacrylate (**PMMA**) and polysterene $(PS))$ are commonly used for the core material of conventional POFs because of their transparency. For radiotherapy dosimetry, all materials of the dosimeter probe should have a nearly water-equivalent characteristic to avoid complicated calibration processes. The mass

densities, electron densities, atomic compositions, mean energy absorption coefficient, and the mean-mass collision stopping powers of the PMMA and PS closely correspond with those of water, as can be seen in figure 2.9.

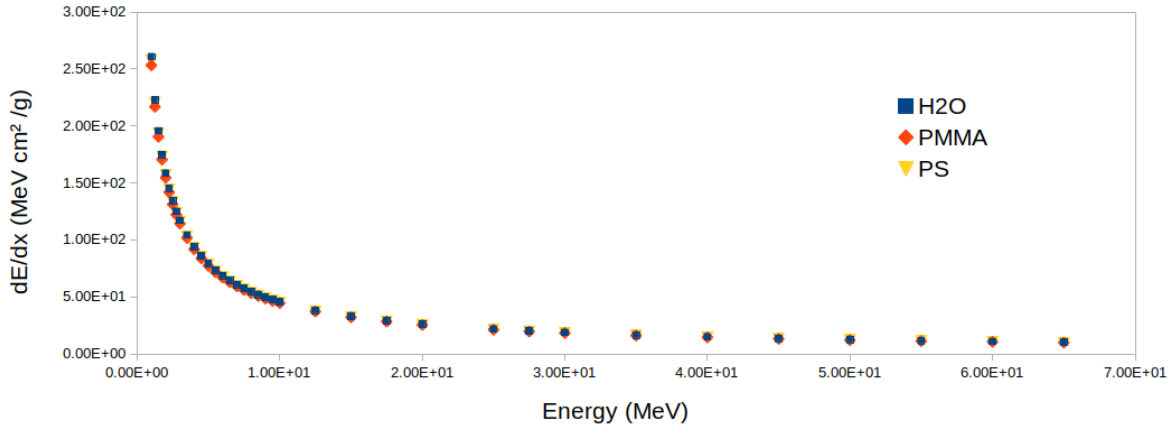

Figure 2.9: The stopping power of a proton beam in water, PMMA and PS. Graph made with the data available in the NIST database [2]

In figure 2.10 it is possible to see that PS has a closer resemblance to water than PMMA.

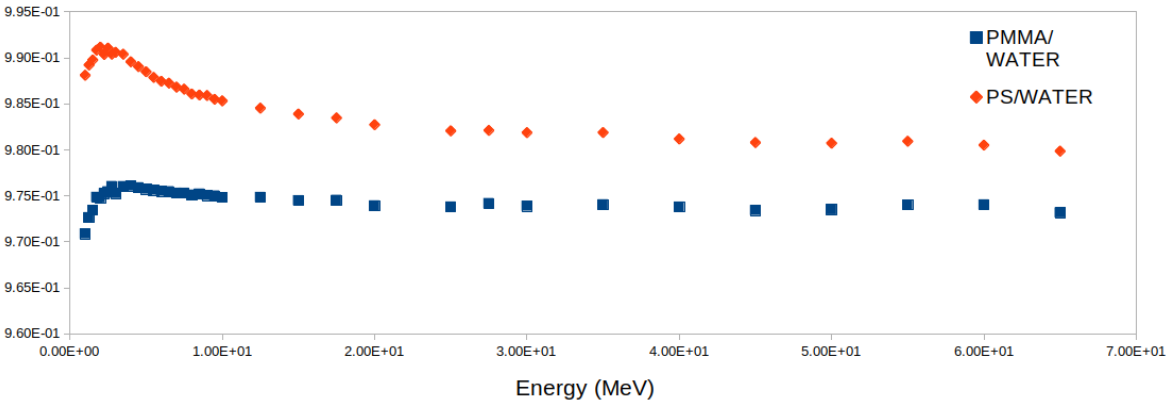

Figure 2.10: The stopping power ratio of a proton beam in PMMA and PS in comparison with water. Graph made with the data available in the NIST database [2]

One of the problems that can be seen in figure 2.10 is that in the area of most interest, the lowest energies, that correspond to the Bragg Peak the ratio isn't constant and that makes it harder to know how the energy read with PMMA or PS correlates with the energy in water.

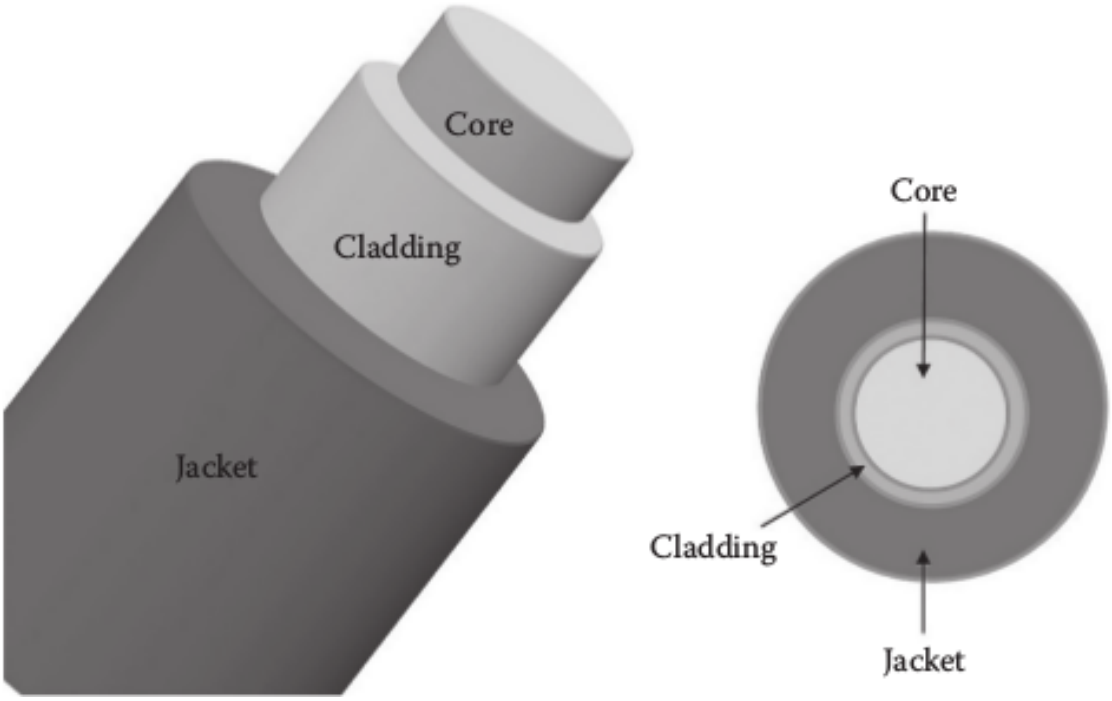

Figure 2.11: The basic structure of an optical fiber [1]. The fibers used in this work only have the cladding and core although a thermo retractable sleeve that resembles the jacket.

2.5.1 OPTICAL FIBERS USED

The optical fibers used during this work were:

- The SCSF-78 from Kuraray with a 1 mm diameter. This optical fiber emits on the blue part of the spectrum, with the peak at 450 nm. It has a low decay time (2.8 ns) and a long attenuation length and high light yield.This type of fiber has a polystyrene core and has a polymethilmetacrylate cladding [25] [26].
- The BCF-10 from Stain-Gobain with a 2 mm diamter. This optical fiber emits on the blue part of the spectrum, with the peak at 432 nm. It has a low decay time (2.7 ns). This fiber consists of a polystyrene-based core and a PMMA cladding [27].
- The BCF-60 from Stain-Gobain with a 2 mm diameter. This optical fiber emits on the green part of the spectrum, with the peak at 530 nm. It has a decay time a higher than the other fibers (7ns). This fiber has a polystyrene core and a PMMA clading [28].

It is important to refer that the fibers used in this work aren't the ones that present the best spatial resolution. Although, fibers with diameters equal to 0.25 mm and 0.5 mm were available. This fibers weren't used because, since only one fiber is used at a time, they produce a small amount of light and they aren't even able to pick up signal in the end of the Bragg Peak, which is the most important part of the beam. The simulations show very clearly this lack of signal.

2.6 PHOTOMULTIPLIERS

A photomultiplier tube, useful for light detection of very weak signals, is a device in which the absorption of a photon results in the emission of an electron. These detectors work by multiplying the electrons by a photocatode exposed to a photon flux, thus creating a current.

Electrons emited by the photocatode are accelerated toward the dynode chain. Focusing electrodes are usually present to ensure that phototelectrons emitted near the edges of the photocatode will be likely to land on the first dynode, and so on. Upon impacting the first dynode, a photoelectron will invoke the release of additional electron that are accelerated toward the next dynode, and so on.

The spectral response, quantum efficiency, sensitivity, and dark current of a photomultiplier are determined by the composition of the photocatode. The best photocatodes are capable of responding to visible light are less than 30 percent quantum efficient, meaning that 70 percent og the photons impacting on the photocatode do not produce a photoelectron. and are therefore not detected [29].

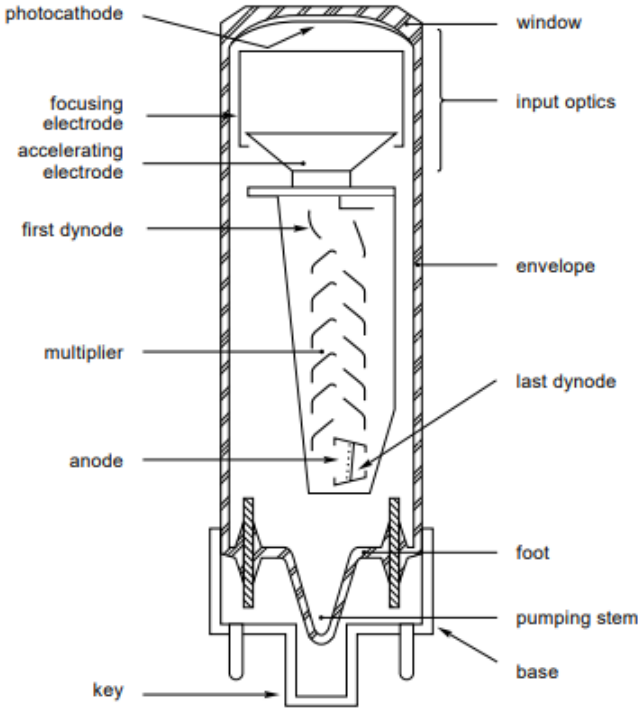

Figure 2.12: Photomultiplier tube scheme [3].

2.7 IRRADIATION BOX

To perform the measurements it was necessary to find a way to keep the room light from interacting with the optical fiber. This is necessary so that all the light the reaches the photomultiplier is light from the scintillating fiber. It was also necessary to make sure that the proton beam can interact with the fiber without being forced to give up a great fraction of this energy before reaching the fiber. With photon radiation a dark sleeve that keeps light out can be used, although, with a proton beam it doesn't work because it doesn't fulfill the second point?. In other words, as a proton interacts with everything in it's path a sleeve will absorb almost all of the energy of a 2 MeV proton beam.

The solution found was to design an irradiation box that consists of a dark chamber, with a piece designed to hold the optical fiber in place and with an aperture to let the proton beam in, this aperture was covered by a window made of silver with a thickness in the order of nanometers so that the proton beam can enter the chamber without giving up too much of it's energy.

The irradiation box was design using LibreOffice Draw [30]. Figure 2.13 shows the design that was proposed to the LIP's offices in Coimbra.

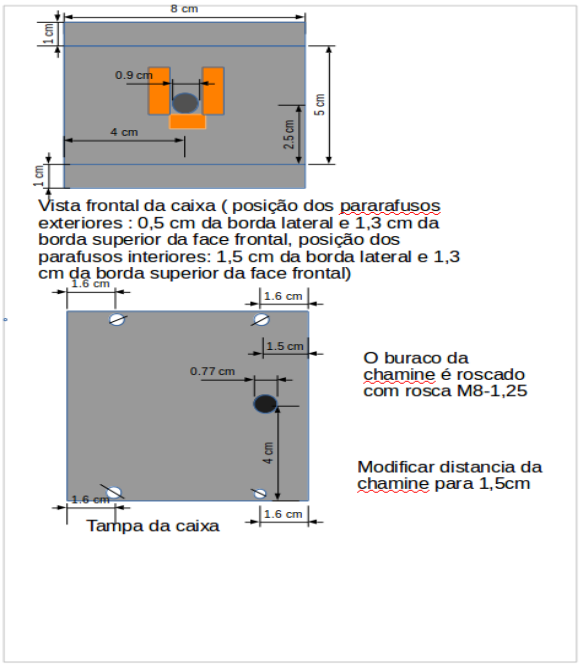

(a) The front face of the phantom. The hole shown in the image is the hole were the proton beam enters the phantom.

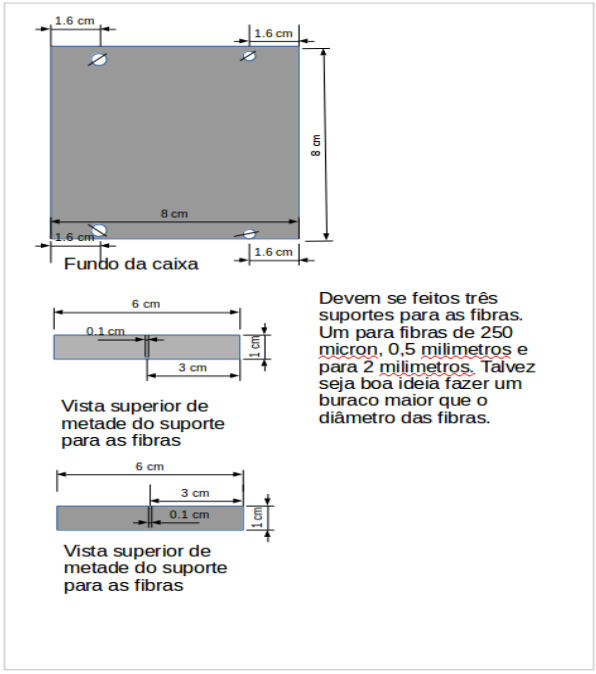

(b) Design of the inside piece that holds the optical fibers

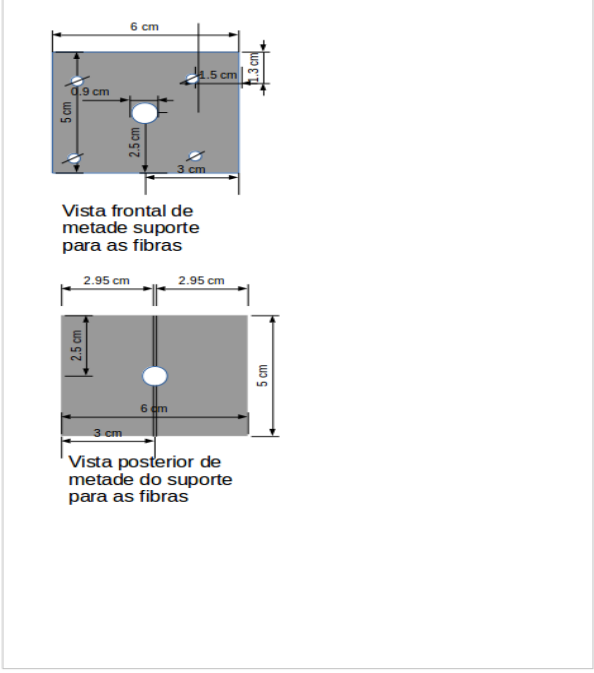

(c) The piece that holds the fiber in place,the screw holes can be seen.

Figure 2.13: Various angles of the phantom. The most important features are shown.

Some changes were suggest by LIP's workshops . Figures 2.14 and 2.16 show the final product, the main changes were made in the piece that holds the optical fibers: in the proposed design the inside piece was composed by two milled piece and in the design proposed by LIP's workshops the inside piece was only one and pierced.

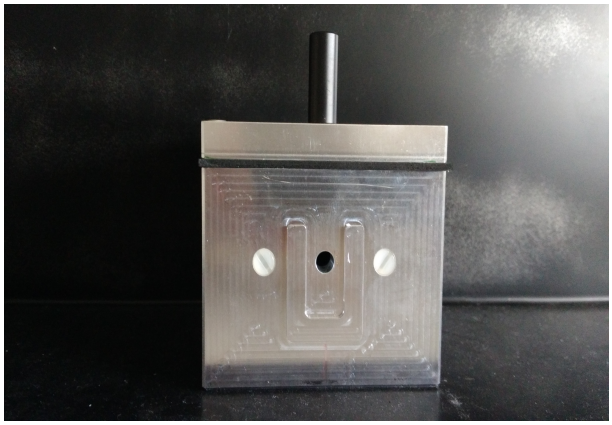

(a) The front face of the phantom. The hole shown in the image is the hole were the proton beam enters the phantom.

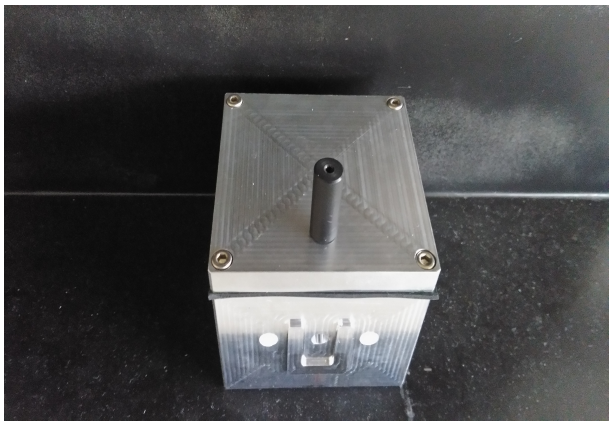

(b) The top view of the phantom.The black piece in the top of the phantom serves the purpose of aiding the entrance of the optical fiber.

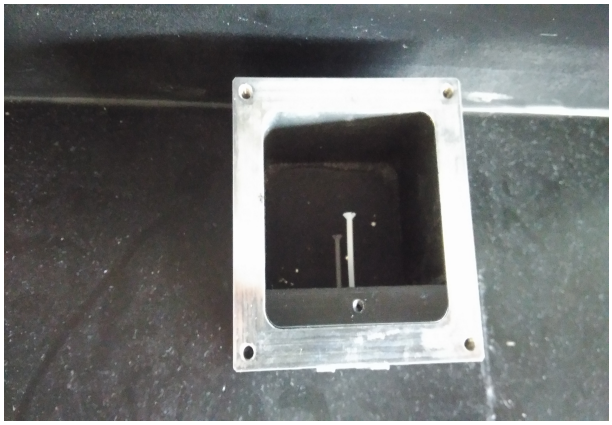

(c) The inside of the phantom. The piece that holds the fiber in place and the screws can be seen.

Figure 2.14: Various angles of the phantom. The most important features are shown.

The windows were made using the evaporator to guarantee that their thickness has low variability.The thickness of the silver window was measured with alpha particles. This method is based on the fact that alpha-particle's energy loss (or any charged particles) while passing through a foil , is proportional to its thickness [31]. If the energy of α-particles entering and leaving the foil is known, its thickness can be approximately determined according to the following expression:

$$l = \frac{(E_0 - E_1)}{\frac{dE}{dx}} \tag{2.10}$$

where l is the thickness from the foil, E_0 is the energy of α-particles entering the foil, this energy depends on the radiation source used on the measurements,in this case the source used was ^{232}U.The decays considered was of ^{212}Po with an energy of 8.7 MeV, E_1 is the energy of α-particles leaving the foil, (dE/dx) is the rate of energy loss for α-particles at an average energy $\frac{1}{2}(E_0 + E_1)$. Using this method we concluded that the silver targets used had a medium thickness surrounding 300 nm. The silver window chosen to perform the measurements was the one with the lowest thickness, as it is possible to see from table 2.1 it is the window with 211 nm. This thickness was also used in the simulations.

Making a simple calculus, using a spread sheet that takes into account the beam's initial energy and the window's thickness, it possible to conclude that the proton beam doesn't transfer much of it's energy to the silver targets, in fact, the energy transfer to the silver windows is in the order of 70 keV, which represents a very small part of the beam's initial energy. It is visible that it is only an approximation because it is considered that the stopping power is constant. This approximation can be regard as good because of the very small thickness of the window.

Window	Thickness
1	211 nm
2	351 nm
3	280 nm
4	422 nm
5	316 nm

Table 2.1: Thickness of the silver windows measured with alpha particles transmission.

Figure 2.15: One of the used windows to block room light. The diameter of the windows is 6 mm.

The material chosen to build the chamber is aluminium. Although,there is the probability that aluminium interacts with the proton beam and forms magnesium ($^{27}Al +^{1} H \rightarrow^{24} Mg + \gamma$), since the reaction has a Q-value of 1600.76 keV and the beam used has an energy of 2000 keV. During the reaction there is a release of γ radiation. If it interacts with the optical fiber will make it produce scintillation light which is indistinguishable from the light produced by interaction between the proton beam and the optical fiber, although the probability of interaction is much smaller. Given that the probability of interaction is so much smaller, this production of γ radiation is negligible ^{24}Mg is stable so it won't emit radiation after the reaction.

The optical fibers are hold on inside of the phantom by a piece designed to receive optical fibers of different diameters, there were produced pieces for 250 μm, 0.5 mm, 1 mm and 2 mm. Each piece has two holes to screw the fibers tight and to stop them from moving. An example of a piece can be seen in figure 2.16b.

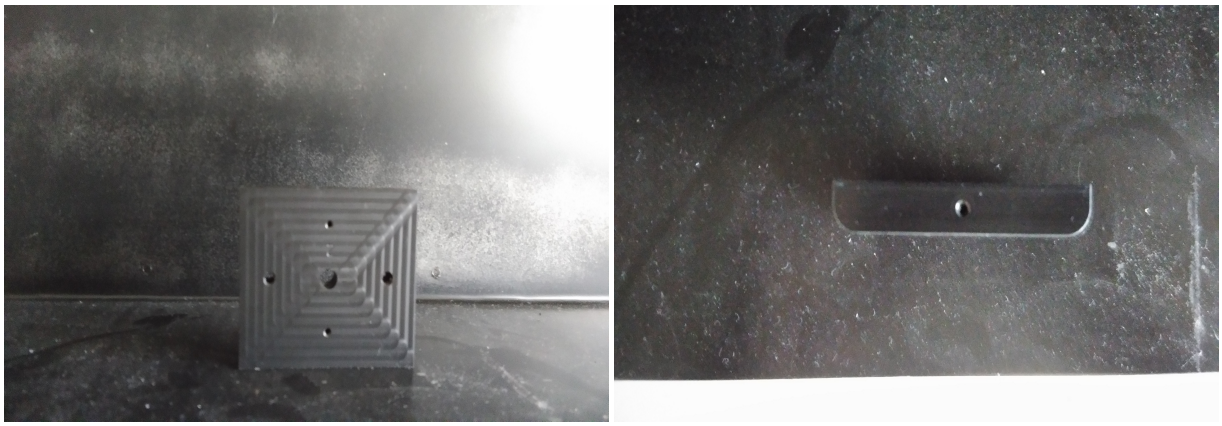

(a) (b)

Figure 2.16: The inside piece that holds the optical fiber in place.

The phantom was manufactured in the LIP workshops in Coimbra.The inside pieces and the outside piece

were made in Polyoxymethylene (**POM**). POM is a cristaline plastic that is used when it is necessary to build a piece design with high precision and high mechanical resistance, it also offers high dimensional stability and a low resistance to movement [32].

The irradiation box was successful in blocking the room light.This can be said because the readout with the accelerator turned off is negligible. But there are some improvements to be made in this system: the system is hard to assemble, the piece inside the phantom to hold the phantom scratches the optical fiber when the fiber is introduced in it, without compromising the production of scintillation light as it only scratches the optical fiber's cladding and not the core, and it is hard to hold the 250 μm and the 0.5 mm with the screws.

2.8 POSITIONING SYSTEM

It was necessary to have a positioning system in the measurements to perform three important tasks. The first was to be able to perform a lateral scanning to determine in what position the optical fiber picked up the most signal,because with this setup it is difficult to be sure that the phantom is perfectly aligned with the exit of the proton beam, the second was to obtain a more precise position for the irradiation box and finally to ensure that the measurement is repeatable.

2.8.1 XY POSITIONING SYSTEMS

To measure the energy deposition of a proton beam it is important to be able to achieve a description of space with a small spatial resolution. The reason for this is that the Bragg Peak has a width in the order of the millimeter. The spatial resolution can be limited by two things, in this work: first the size of the optical fiber, but in our work won't be a problem because we use optical fibers with 2, 1 and 0.5 mm; the second is the quality of the positioning system. To achieve a good position precision a xy system can be used. A xy system is a set of two arms each one with a belt connected to a stepper motor that allows to move something along two axis, the precision that a xy system offers depends on the precision that the motors are able to offer.

The motors used in a xy system are electrical stepper motors. A stepper motor is an electromecanic actuator that converts electric signals in precise angular displacements The stepper motors don't work with a feedback loop, that means that the motor doesn't return to the previous position, after it receives a command it moves to another position and it stays in that position.

2.8.2 ELECTRICAL MOTORS

The NEMA 17 motors we will be using in this work are Hybrid Stepper Motors. This type of stepper motors have a small angular step equal to 1.8^o, that corresponds to a 0.4 mm resolution. The hybrid motor has a rotor with a permanent magnet, with two polar bodies, with teeth. The stator typically has two windings with several reels and magnetic poles also with teeth.

Being the rotor of a hybrid motor constitute by polar bodies coupled to a permanent magnet, these bodies have polarity, a north and a south pole.

The figure 2.17 illustrates how a stepper motor works:

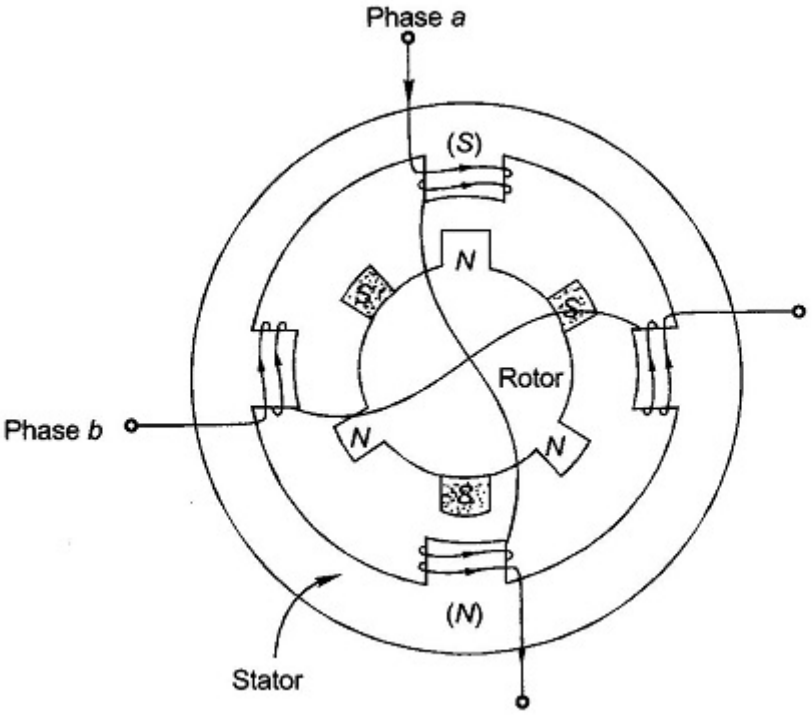

Figure 2.17: Stepper motor scheme.

- First step: When the winding A is charged it is created in the superior teeth a north pole that attracts the south pole of the rotor and in the inferior teeth the south pole attracts the north pole of the rotor.
- Second step: When the winding B is charged it is created a north pole in the right teeth that attracts the south pole and in the left teeth is created a south pole that attracts the north pole of the rotor.
- Third step: to continue moving the rotor in the clockwise direction (like in the image) a current passes through the winding A in the opposite direction to the one in the first step. With this happening the top teeth becomes the south pole and the bottom teeth becomes the north pole. So that the south pole of the rotor is attracted to the inferior teeth and the north pole is attracted to the superior teeth.
- Fourth step: the same is done in the B winding. The current goes through the winding in the opposite direction of the one in the second step. And the south pole of the rotor is attracted to the left teeth and the north pole of the rotor is attracted to the right teeth.
- Fifth step: The process is repeated so that the rotor continues moving.

The NEMA 17 stepper motor is also a a bipolar stepper motor, which means they have two equal windings, where the current flows. The phantom is placed on the metal plate in figure 2.18.

2.8.3 POSITIONING SYSTEM USED

The positioning system used is the model XY-9 from Arrick Robotics [4]. With an axis travel distance of 23 cm. As can be seen in figure 2.18 this positioning system as two independent axis, each one with it's own motor.

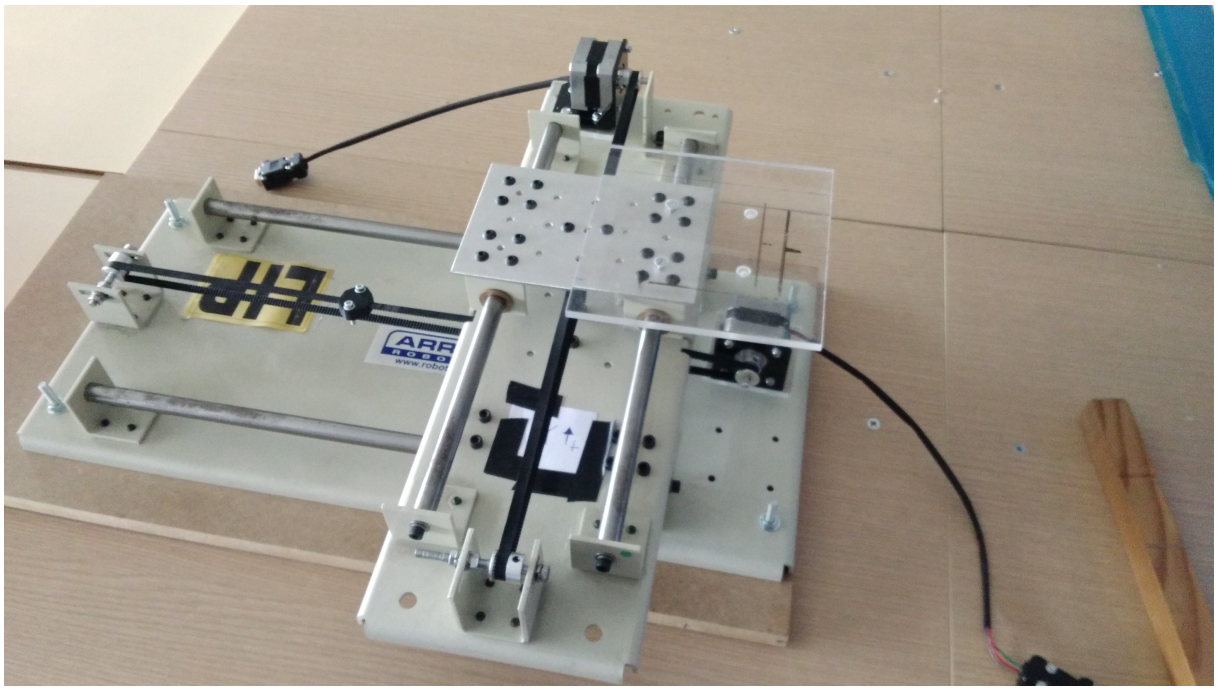

Figure 2.18: The XY-9 Arrick Robotics positioning system [4], with the new motors, the new timing belt and the platform

The original driver to control the motors that were used in the positioning system was not found, but the team found a driver made by a former student. With that driver it was possible to make the motors run and so to make the positioning system work. Nevertheless, because of the way the driver was built it had several problems:

- The fact that with the voltage the motors are suppose to work with, 20 V, there was the risk of burning the LED's in the driver because they had to deal with a high potential difference;
- the driver had a set of MosFET (8, 4 for for each motor, 1 for each coil of the motor) conducting when the respective motor was on standby that would increase the current consumed by the driver and it would lead to an increase in the temperature that in a long session could be harmful for the driver.

Because of these problems the decision was made to buy another driver. With the new driver the standby consume lowered to 5 mA and the working current lowered to 200 mA, while the former driver consumed the maximum current allowed by the current source used.

The system was rehabilitated buying a new set of motors that were compatible with the new driver: the Adafruit Nema-17 Stepper Motors together with the Adafruit DC & Stepper Motor HAT [5] to control the motors, this HAT is controled by a Raspberry Pi 3B+ [6], wich is a microprocessor.With the new motors the system achieved a step resolution of 0.4 mm. The step resolution was determined through measurements done with a fixed number of steps and measuring the distance traveled by the axis.

The script to control the motors was developed using the library provided by Adafruit. The script was developed, not only to control the motors but also to keep track of the position in which the phantom is.

There were a number of structural changes made to the positioning system in order to accommodate the new motors, new timing belt and new timing pulley. A platform, seen in figure 2.18 was also added to the positioning system to allow for the phantom to get closer to the exit of the proton beam, so that the first centimeters of beam were able to be read.

Nevertheless, the rehabilitation wasn't a total success because the Nema-17 Stepper Motors don't offer enough torque to move the heaviest axis of the system more than 10 cm. This isn't a problem for the presented experimental setup because, as was stated the 2 MeV proton beam in air only travels 7 cm. That being said, during the experiments,

after a lot of use the motors weren't able to move the heaviest axis, which was being used as the axis parallel to the beam's exit, more than 6 cm, this may be due to the fact that during all the measurements the timing belt may have gotten looser.

Figure 2.19: Adafruit DC & Steppermotor driver [5] mounted on the Raspbery Pi 3B+ [6].

2.9 PROTON ACCELERATOR

The proton accelerator used during the experiments was the Van de Graaff [33] accelerator, that belongs to CTN, that can produce a 2 MeV beam with a variation between 5 % and 10 % . At CTN, the Van de Graaff accelerator has multiple branchs and the one that was used is the microprobe, that emits a very thin beam. The beam intensity could work in the range of $0 - 1000\ pA$.

The Van de Graaff is a type of high-voltage electrostatic generator that serves as a particle accelerator. It works by building and maintaining a high potential difference on a smooth conducting surface by the continuous transfer of positive static charges from a moving belt to the surface. When used as a particle accelerator, an ion source is located inside the high-voltage terminal. Ions are accelerated from the source to the target by electric voltage between the high-voltage supply and ground [34].

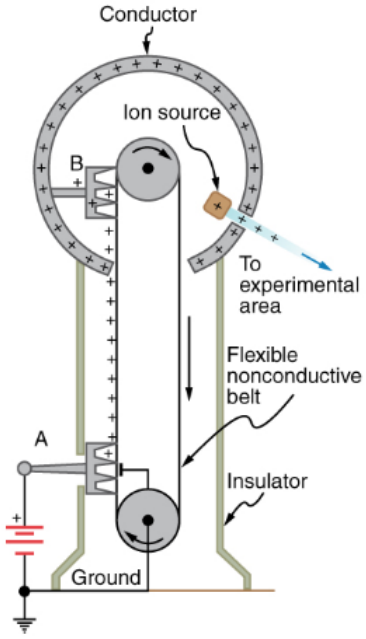

Figure 2.20: The Van de Graaff accelerator [**?**]

One of the main problems found in the CTN's system is that one cannot, during measurements, directly know the intensity of the beam being emitted and, besides that, the beam isn't stable which means that it's intensity can vary over time. This is noticeable by the fact that sometimes, at the same position, the readout would be different. This ruined some series of measurements because when the intensity increased the readout electronics would go into overload and it's voltage needed to be lowered.

2.10 EXPERIMENTAL PROTOCOL

The protocol designed to perform this experiment:

1. With the phantom as close as possible to the exit of the Van de Graaff, start the measurements with the hole in the box as much aligned as possible with the exit of the Van de Graaff accelerator.
2. Perform a lateral scan and register the measurements in various lateral positions. Find the position with the maximum signal and define that as your control position.
3. Move to another longitudinal position and perform the lateral scanning.
4. Return to the control point.
5. Continue the measurements in another longitudinal positions, always returning to the control point.

Each measurements involves a 15 second current integration in the electrometer.

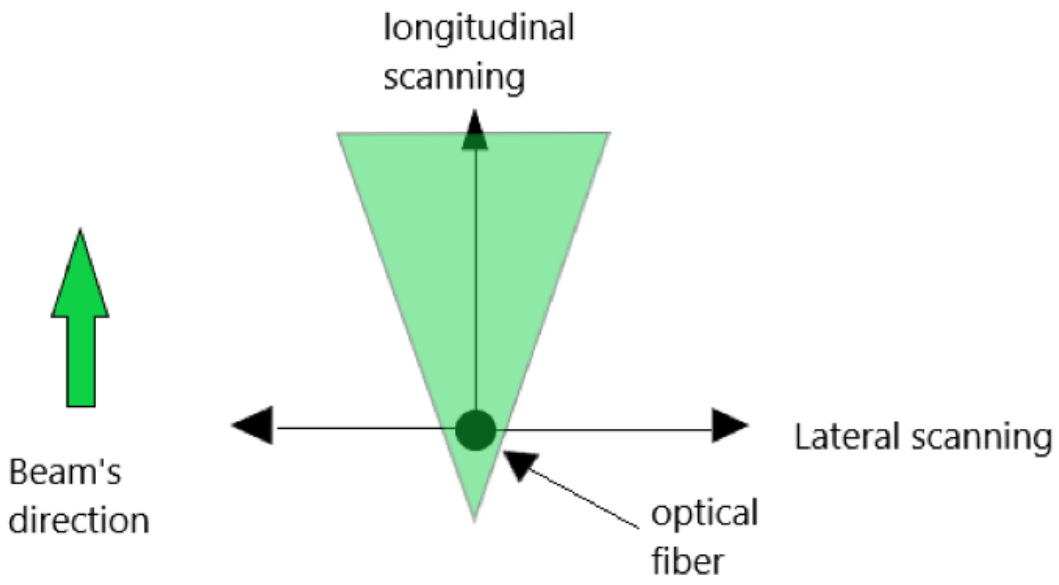

Figure 2.21: The motion described by the optical fiber.The pale green cone represents the beam's divergence

It was chosen to perform a lateral scan for two reasons: the has to do with the fact that it is impossible, with the current setup, to guarantee that the optical fibers are perfectly aligned with the beam's exit point and searching laterally for the point with most signal we can consider that signal as the reference for the longitudinal point the fiber is in; the second is that performing the lateral scan it is possible to determine the beam divergence, and that will make the simulations better because that information will be introduced in the beam's geometry.

2.11 SIMULATIONS

2.11.1 MONTE CARLO SIMULATIONS

In order to have an idea of what to expect from the experimental measurements it is important to perform simulations. In the case of this work, simulations will also be important in order to be able to extract the Birk's coefficient for the studied scintillators. With that in mind it is very useful to perform Monte Carlo (MC) simulations to recreate the experimental conditions.

Monte Carlo simulation techniques involve sampling at random to artificially simulate a large number of experiments and to observe the results, because of this, MC can be used to solve any problem with a probabilistic interpretation. In other words, the core idea of MC is to learn about a system by simulating it with random sampling [35].

To perform a Monte Carlo simulation it is of up most importance to have a good random number generator. In practice numerical simulations need random number generators to set up initial conditions or to generate new configurations. In fact, there is no such thing as a random number generator, as Jonh Von Neumann (1903-1957) said :"Anyone wishing to produce random numbers with a computer is truly in a state of sin". What random number generator really is a pseudo-random-number-generator that can produce a long sequence of numbers that can imitate a given distribution. The random number generators used in particle transport algorithms follow a probability density function. This probability density function can be used to represent many things: from the distribution of energy that the particle's generated have, to the probability of an interaction occurring or even the distribution of the energy transferred in each interaction [36] [37].

2.11.2 PARTICLE TRANSPORT ALGORITHM AND CODES

Particle transport is based on cross sections (i.e., interaction probabilities) per unit distance, and because of that it can be described by stochastic processes. In a transport simulation, at each step of the particle through the geometry, the probability density function is representing the probability of physics interactions and their outcome [15].

A Particle Transport Algorithm depends on the particle's history. This history can be defined as the knowledge of the particle trajectory, including potential secondary particles.

When simulating a number of particle histories, one first generates the original particle source. The simulation of the source defines the beams initial conditions: the beam's direction, spread (one can have a pencil beam, where all particles exit the source in a straight line, or one can have a beam with a certain divergence) and initial energy (that can follow a certain distribution or have a fixed value). The particle tracking is performed by simulating the passage of particles through a well-defined geometry, one particle at a time, one step at a time, randomly sampling from one or more probability distributions at each step in order to choose how the particle might interact in a way consistent with the laws of physics.The step size is important to the outcome of the particle tracking algorithm. It should be small in such a way that there isn't much difference between the cross sections at the beginning and the end of the step is small.

For charged particles it is very ineffective to simulate all the physical interactions because these type of particles, like protons, interact many times. For example, energy losses and directional changes are condensed into a single step. Multiple-scattering theories provide probability density functions that represent the net result of several single-scattering events.

When a radiation transport simulation is performed some things other than the physics have to be defined : the tracking geometry, the materials involved, the particles of interest, the generation of primary events, the response of sensitive detector components, the generation of event data, the storage of events and tracks, the visualization of the detector and the particle trajectories, and the analysis of simulation data at different levels of detail.

2.11.3 FLUKA

Fluka was taken as the reference software for the simulations, more specifically the 2011.2x.06 version [38], it was used to perform calculations and to compare them with the experimental data, but also to validated the simulations made with pMC.

It is to refer that there are some discrepancies between the predictions made with FLUKA and the predictions made with pMC. As is visible from figure **??**. It is important to notice that while pMC uses the NIST database for Stopping Powers [2], FLUKA uses another Stopping Power database, besides that the scattering algorithm for pMC takes the particles forward while with FLUKA they scatter a lot more side ways.

The simulations used to compare pMC and Fluka were very similar: both considered a pencil like proton beam, with a void filled with air and an optical fiber with 1 mm and 2 mm diameter with 6 mm weight, this weight corresponds to the diameter of the hole in the phantom. The silver window was included in both simulation and was considered a thickness of 211 nanometers.

The simulations in FLUKA were made with the HADROTHE (Hadron Therapy) default. The geometry was defined using the materials available in the FLUKA database, no new materials were defined. The scoring was made using the USRBIN card with the REGION scoring, this calculates the energy deposited in GeV/cm^3 what means that the energy should be multiplied by the volume of the body considered.

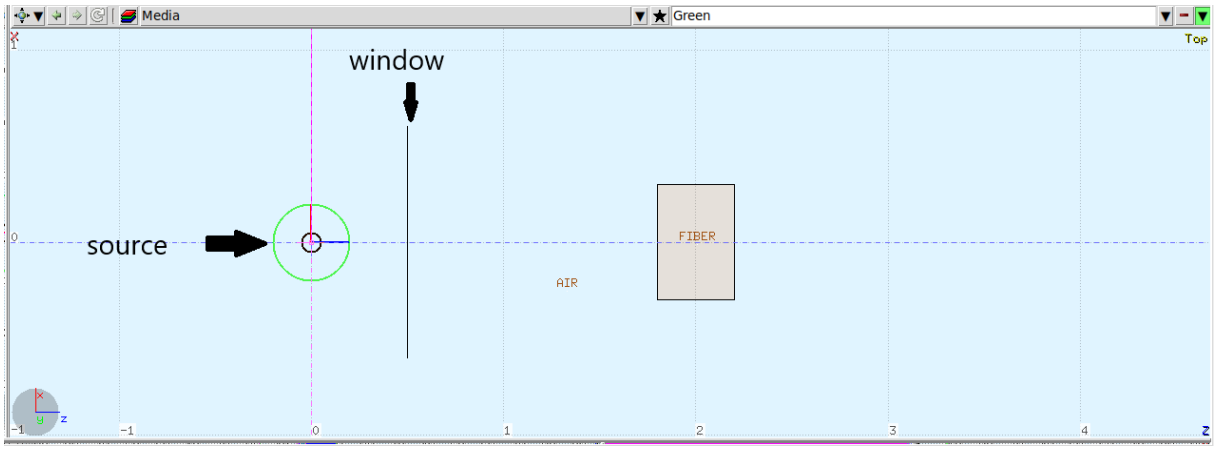

Figure 2.22: Screnshot of the FLUKA geometry display displaying the simulation of the experimental setup.

2.11.4 pMC

The pMC software is an adaptation of the alfaMC software [39], made during this work. This software is only used in a range of energy between 1 and 15 MeV, because this software only considers Coulomb interactions.It allows simulations 100 times faster than the simulations in FLUKA or SRIM [40] and it allows for the quick computing of geometry by combining predefined volumes.

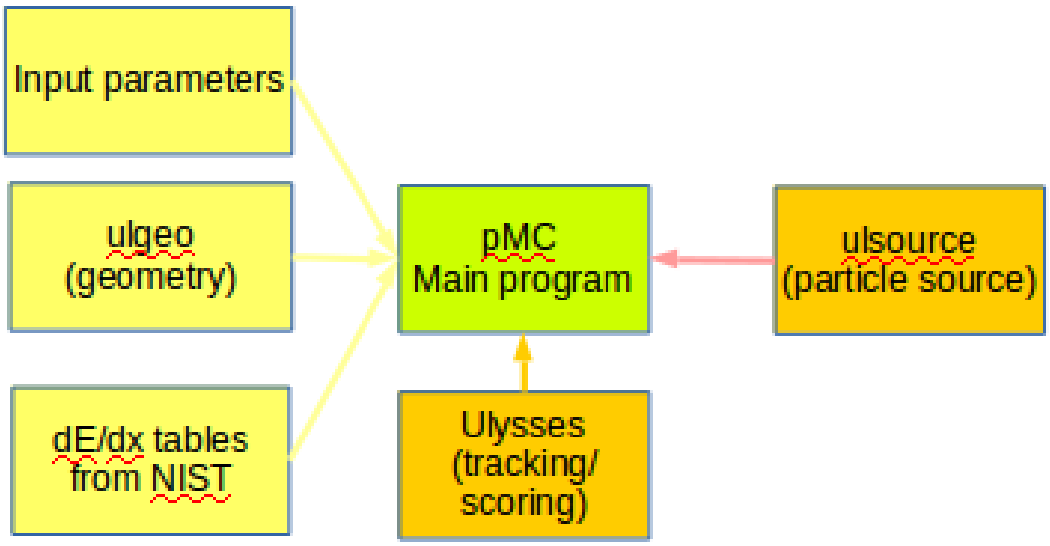

Figure 2.23: Block diagram that shows the architecture of pMC.

Ulisses is the routine that defines the tracking and scoring of pMC.

The adaptation was made through certain changes and the adding of some features to the alfaMC software:

- The software stopped considering particles with the mass and charge of alpha particles and started considering particles with the mass and charge of protons.
- The energy transfer for thin sheets was calculated through the Vavilov distribution transfer and the energy transfer for not so thin sheets was calculated through the Landau distribution.

Regarding the modifications specific for this work, certain changes were made to account for different types of geometry, beam and scoring:

- The geometry of the software was changed to accommodate the presence of the silver window and to enable the user to choose not only the traveling of the optical fiber in the direction perpendicular to the proton beam but also in another directions, in other words, the optical fiber can now travel in directions perpendicular to the beams direction. This is important to check if the phantom misalignment and the beam divergence can explain the results obtained.
- A routine was added so that the software can calculate the response taking in to account the Birk's quenching model.
- The beam's geometry was adapted to follow a Gaussian distribution.
- The scoring was changed to be able to calculate not only the energy absorbed per number of primaries simulated but also the energy deposited per number of primaries that interacted with the optical fiber.

As the simulation were suppose to be as close to the experimental setup as possible certain consideration were made: the silver window was added to the simulations, only a small volume of optical fiber, corresponding to the volume exposed to the beam, was considered. So the simulation consists of:

- a small cylinder with 6 mm of diameter and a height of 211 nm with the main axis parallel to the beam's direction. This cylinder corresponds to the window used in the in the phantom and so it was made of silver;
- a cylinder with 1 or 2 mm of diameter (depending on the optical fiber simulated) and a height of 6 mm with the main axis perpendicular to the beam's direction. This cylinder corresponds to the optical fiber and so it was composed by PMMA or polystyrene, depending on the optical fiber simulated;
- air, which is the mean that involves these two cylinders.

3 RESULTS ANALYSIS AND DISCUSSION

During this work were performed two sets of measurements. The first set was performed in January 2019 and the second set was performed in June of the same year. The results from these two sets of measurements will be presented separately, because in the second set of measurements the positioning system was used, which enabled the extraction of a totally different set of data that regards the divergence of the beam and the analysis of it's geometry.

3.1 SIMULATIONS

Three different MC programs were employed: FLUKA, pMC and SRIM. Here FLUKA is taken as the reference software.

Figures 3.1, 3.2, 3.3 shows how pMC compares with Fluka and SRIM in the simulation of the interaction of a proton beam with air. The values chosen correspond to the energies of the Van de Graaff accelerator (2 MeV), the Tandem (4 MeV) and the ICNA'S cyclotron (13 MeV).

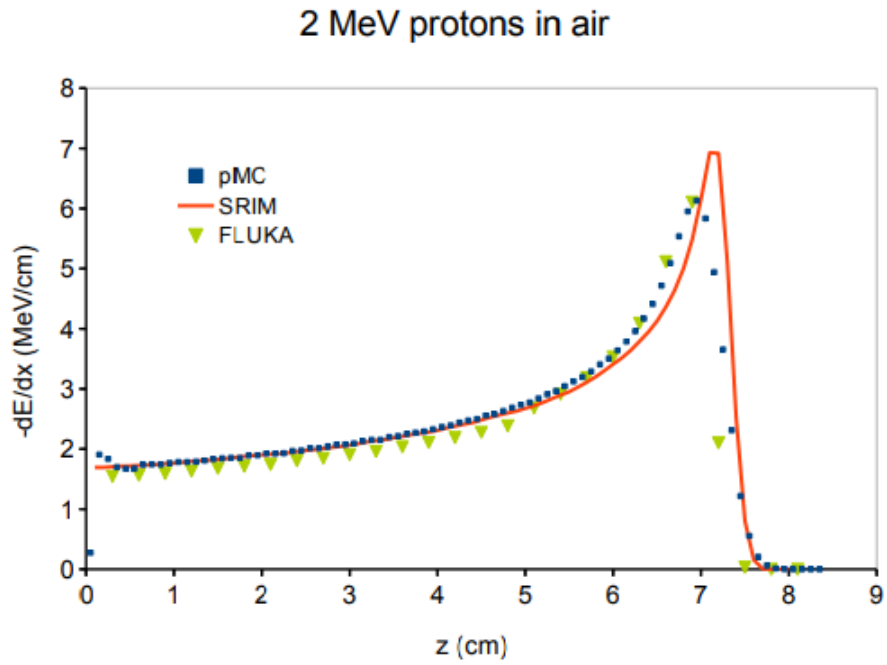

Figure 3.1: Bragg Peak simulated with pMC, FLUKA and SRIM for a 2 MeV proton beam

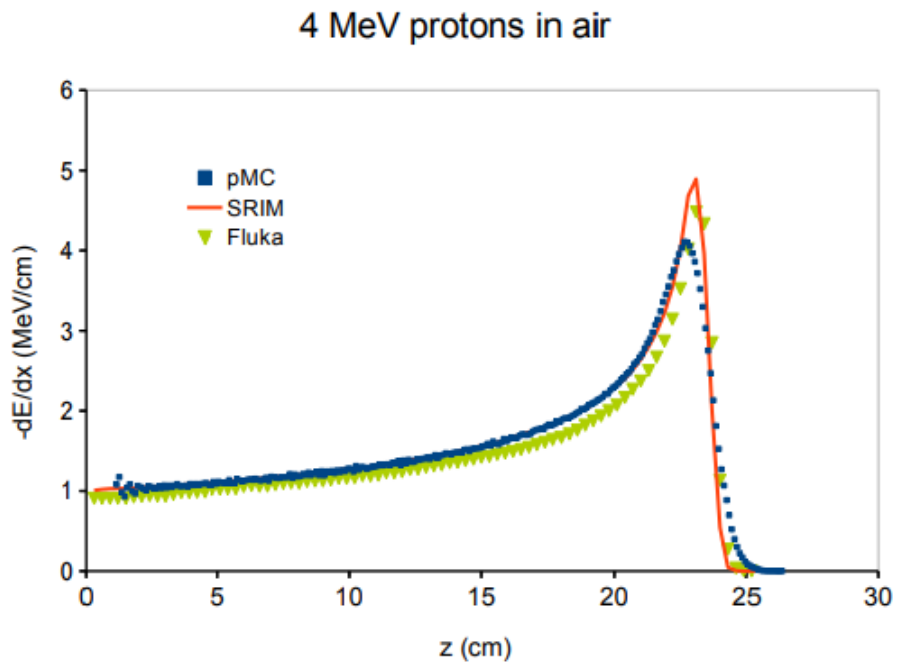

Figure 3.2: Bragg Peak simulated with pMC, FLUKA and SRIM for a 4 MeV proton beam

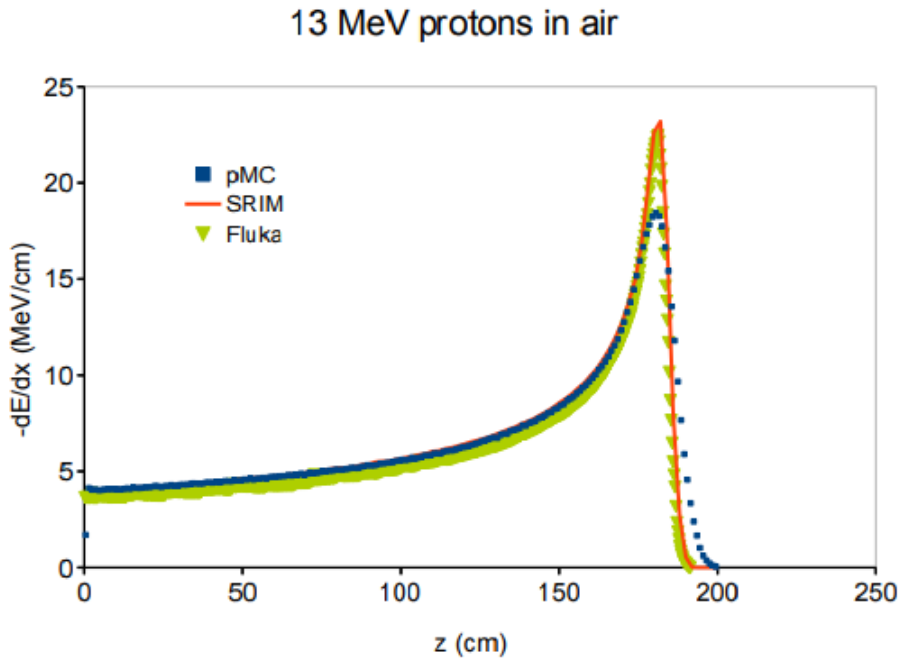

Figure 3.3: Bragg Peak simulated with pMC, FLUKA and SRIM for a 13 MeV proton beam

Figure 3.4 shows the comparison between the energy absorbed by an optical fiber calculated using Fluka and using pMC, for a 2 MeV proton beam. The simulation was performed to compare the two MC programs in the variable that is measured in the experiment.

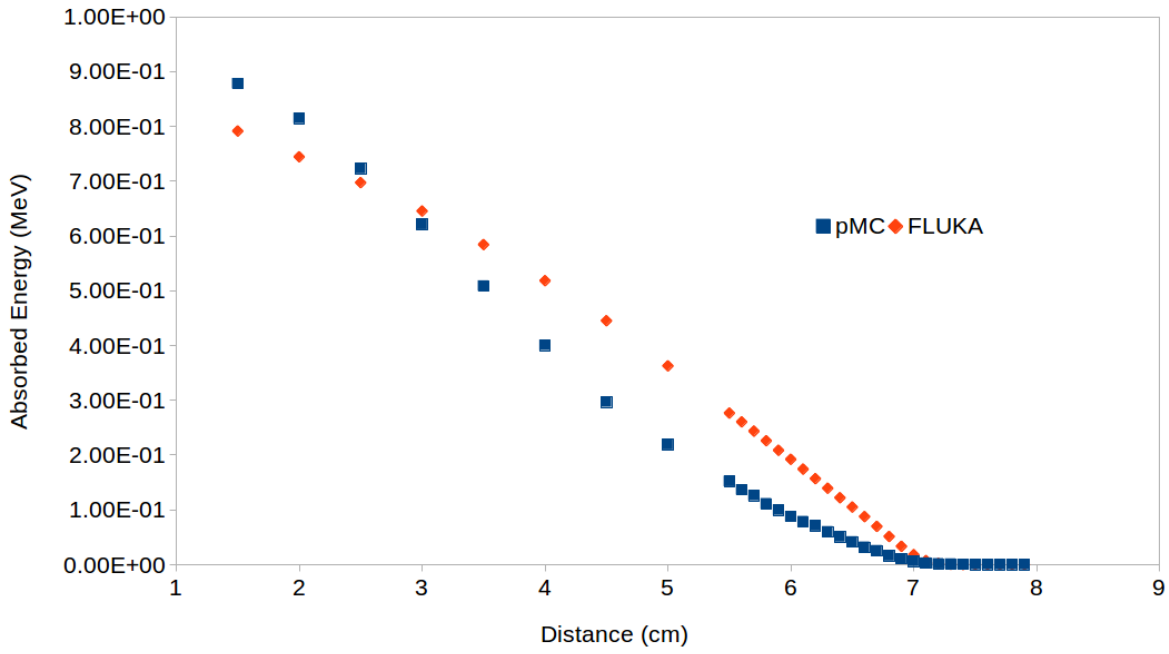

Figure 3.4: Comparison between the energy absorbed by a 2 mm optical fiber at a 2 MeV beam using Fluka and pMC.

It is observable that with pMC the Bragg Peak doesn't reach stopping powers as high as FLUKA or SRIM (this is visible in the height of the Bragg Peak in figures 3.1, 3.2 and 3.3), but the protons have a bigger range than in FLUKA and SRIM. It is also visible in 3.4 that in Fluka the proton beam deposits more energy in the fiber. In figure 3.4 it is also visible that the optical fiber absorbs energy at a greater distance in the simulation performed with pMC. This phenomenon can be explained by the scattering model used in pMC, as it makes the protons scatter with a small lateral component. Other explanation for the the discrepancies found has to do with the fact that pMC uses the NIST database [2] for the stopping powers and Fluka uses it's own database.

It is important to refer that although it will take more work and some more comparisons to establish the accuracy of pMC this software was very useful during the development of this work. This is true because it enabled the performance of simulations that were fast and free of constraint from predefined functions, like what happens with FLUKA.

3.2 First Set of Experimental Measurements

The first set of measurements was performed with the BCF-10 and the BCF-60 optical fibers. The positioning system present at CTN was used, which is manual. On the CTN's Van de Graaff it is not possible to know the beam's intensity, while measurements are being performed. For this reason it is completely impossible to estimate the number of protons that interact with the optical fiber. This can't be transported to the simulations for intensity normalization. So, all the results will be presented normalized with regard to it's highest value, even the simulations.

3.2.1 Longitudinal Experimental Measurements

The figure 3.5 shows the results of the longitudinal measurements performed at CTN for the BCF-60 optical fiber. The measurements were performed with a the photomultiplier with it's voltage set to 700 V, this voltage was choosen so tha the electrometer wouldn't reach saturation, and the Van de Graaff current was set to 200 pA.

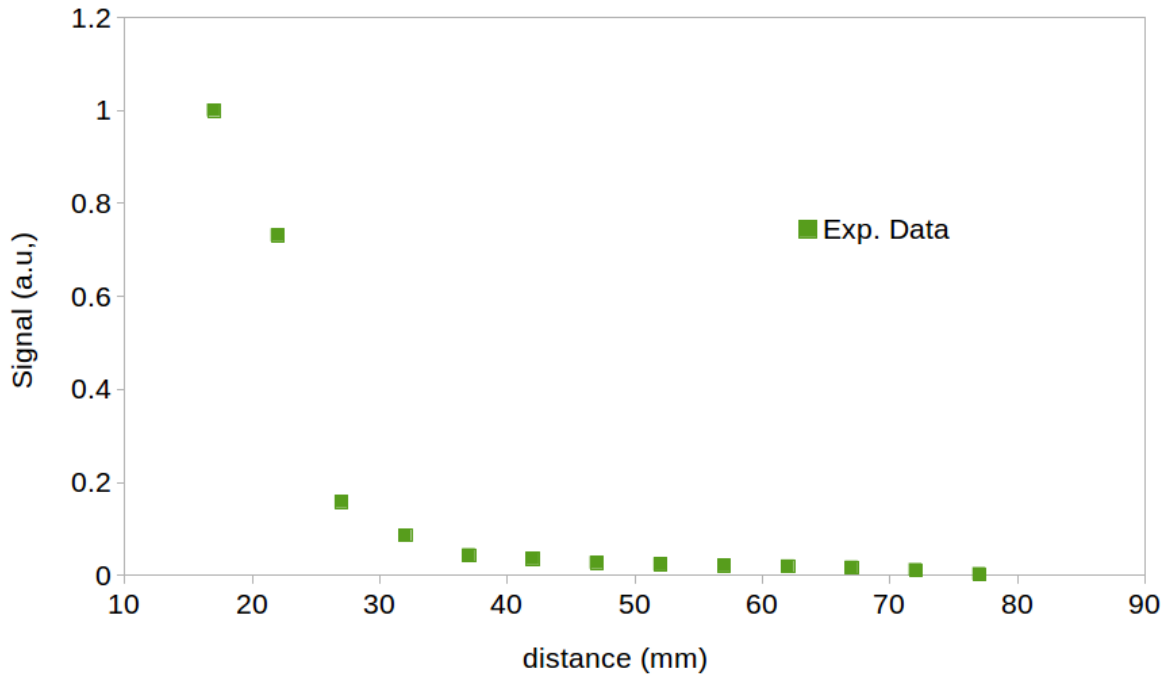

Figure 3.5: Signal obtained in a 2 mm fiber at the 2 MeV proton beam at the CTN Van de Graaff. The longitudinal profile is obtained in air.

The first measurements performed in January 2019 at CTN's Van de Graaff gave results that showed that it would be more difficult than expected to measure and map the beam's Bragg Peak.

Certain difficulties were encountered: the first was to align the phantom's aperture with the beam's exit, the second was to make sure that the optical fiber stayed perfectly aligned with the beam's exit because with the irradiation box used in these measurements the optical fiber wasn't fixed with screws.

During the measurements was discussed the idea of performing a lateral scanning in order to identify the position where the beam presented the most intensity. With the positioning system that was available at CTN was not possible to perform the lateral scanning. Because of that, the first measurements only account for a longitudinal measurement.

The measurements were confirmed by the simulations. Figure 3.6 shows the comparison between the experimental measurements and the simulations performed with and without the alignment of the beam with the beam's exit. It is possible to see that introducing in the simulation the fact that the optical fiber is dislocated from the beam's center better explains the experimental measurements. The fiber, when the user chooses to displace it in relation to the beam's exit,follows a track dictated by:

$$y = z_{tar} \cdot \tan(\theta \cdot \pi/180) \tag{3.1}$$

where y is the y coordinate of the silver window's position (the fiber's position is defined as a function of the window's position, z_{tar} is the z coordinate of the window's position, $z_{det} = z_{tar} + 1.5$ (the addition of 1.5 cm is necessary because of the thickness of the phantom) and θ is the angle chosen by the user to displace the optical fiber.

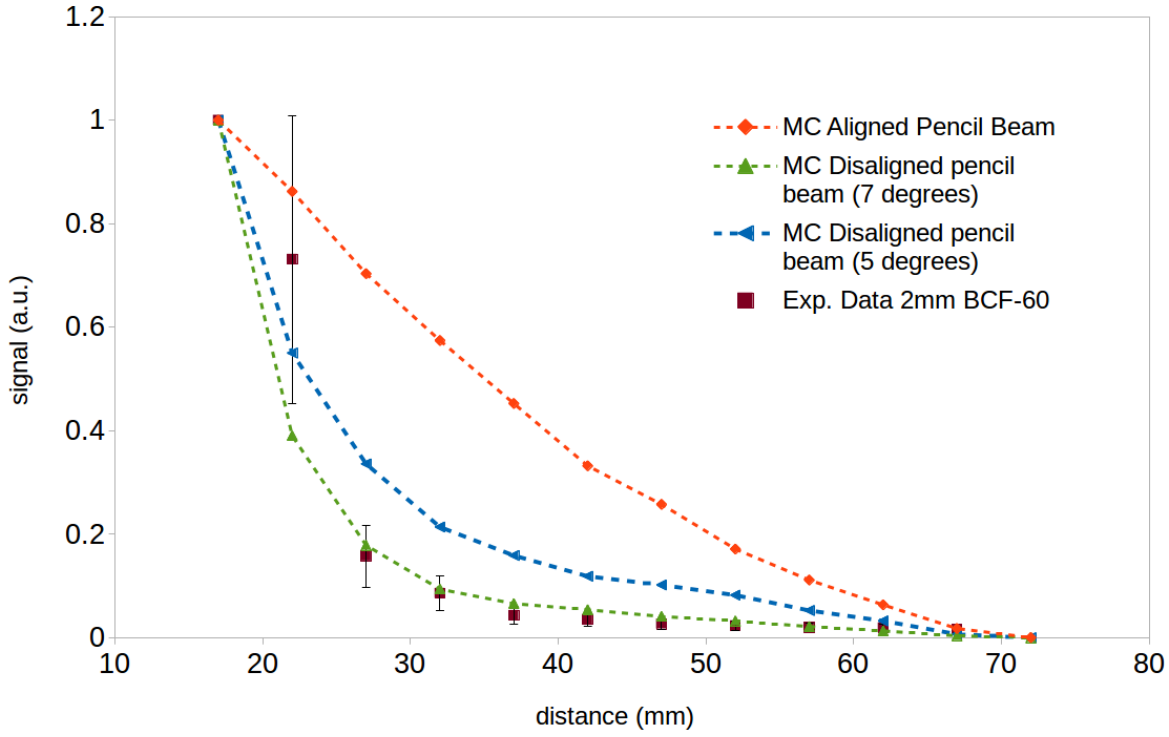

Figure 3.6: Experimental results of the BCF-60 fiber compared with the simulations performed on pMC. One of the simulations was with the optical fiber perfetly aligned with the beam's exit and a pencil beam and the other was with an angle of displacement equal to 5 degrees in the horizontal plane and a pencil beam.

The possibility of having the Birk's factor was added to pMC and simulations were performed considering quenching. Figure 3.7 shows the result of these simulations.

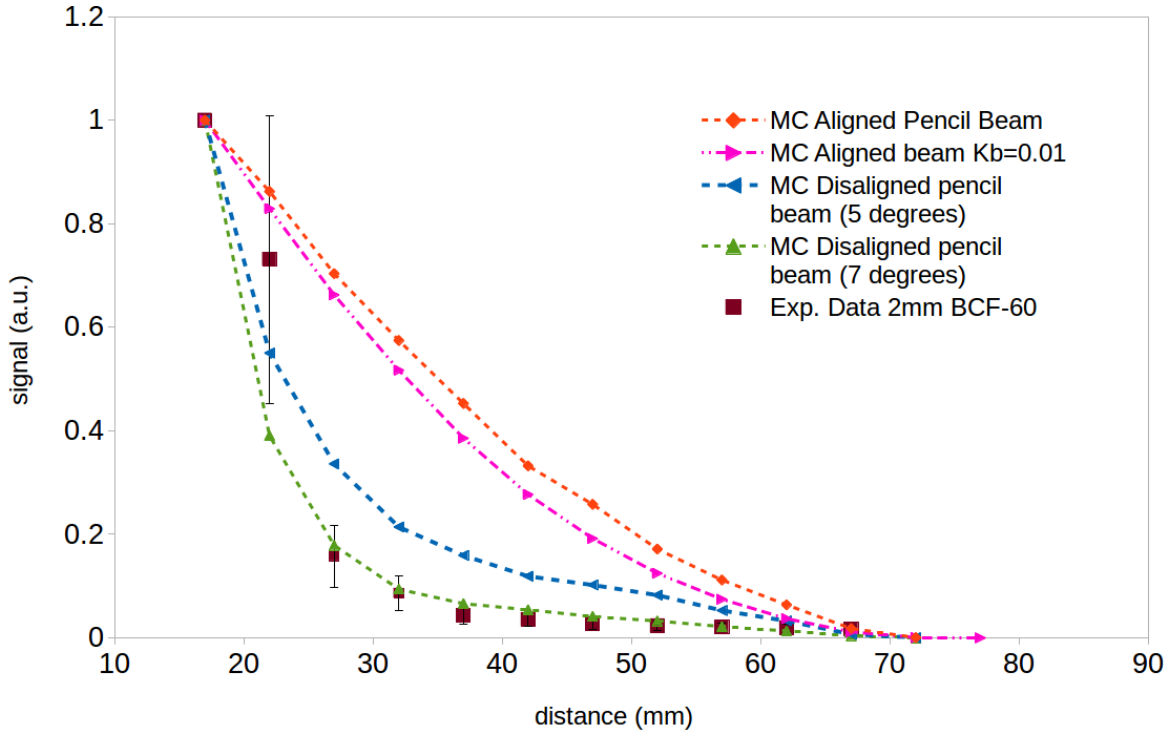

Figure 3.7: Experimental results of the BCF-60 fiber compared with the simulations performed on pMC. One of the simulations was with the optical fiber perfetly aligned with the beam's exit and a pencil beam and the other was with an angle of displacement equal to 5 degrees in the horizontal plane and a pencil beam, considering also the Birk's formula.

The simulations showed that the experimental points don't have the quality necessary to extract the fiber's birk's coefficient

3.3 SECOND SET OF EXPERIMENTAL MEASUREMENTS

3.3.1 BEAM'S DIVERGENCE AND GEOMETRY

A second set of experiments was performed by the reasons already stated: the fact that it is impossible to guarantee that the fiber is perfectly aligned with the beam's exit made it compulsory to perform the measurements with the XY positioning system to perform a lateral scanning. This set of measurements was performed with the 1mm SCSF-78 optical fiber from Kuraray and with the 2mm BCF-12 optical fiber from SaintGoban.

Figures 3.8 and 3.9 show the lateral profiles measured for various distances (regarding the beam's exit), for a 1 mm and 2 mm optical fiber, respectively.

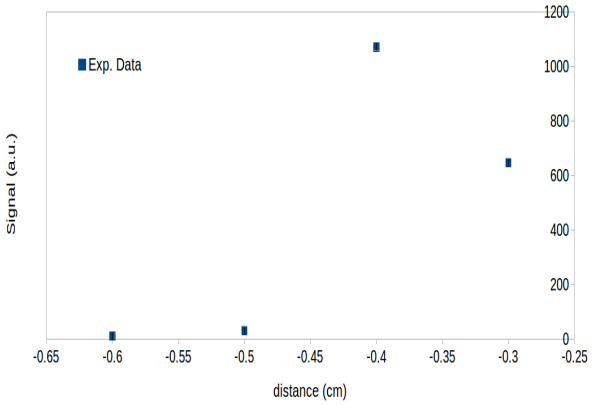

(a) distance:1.5 cm

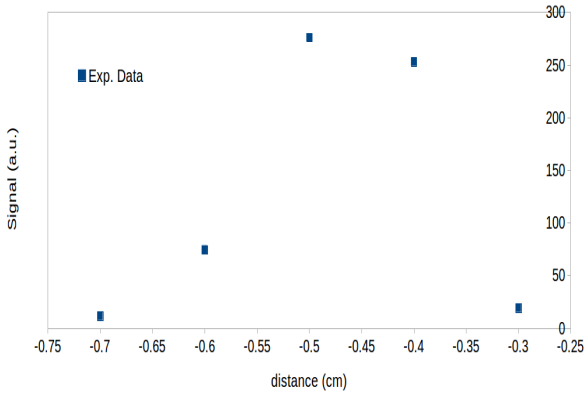

(b) distance: 2.5 cm

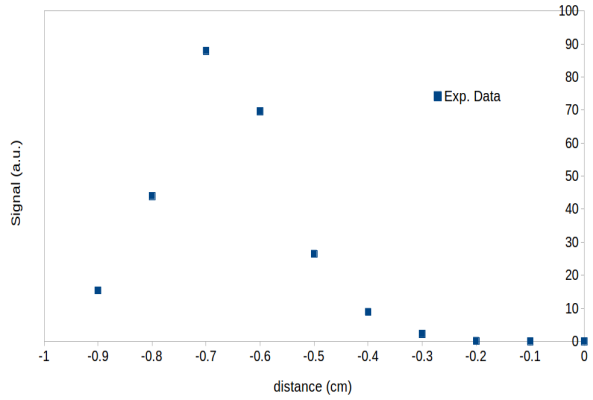

(c) distance: 3.5 cm

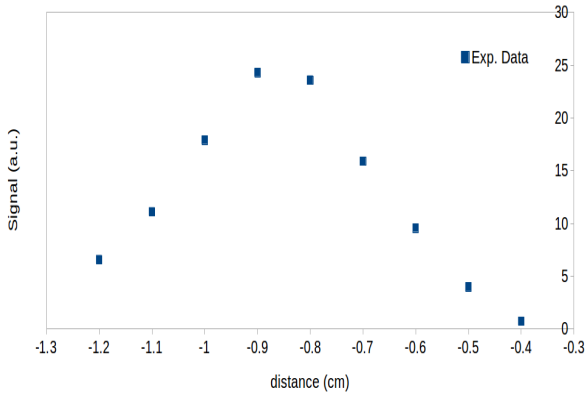

(d) distance: 4.5 cm

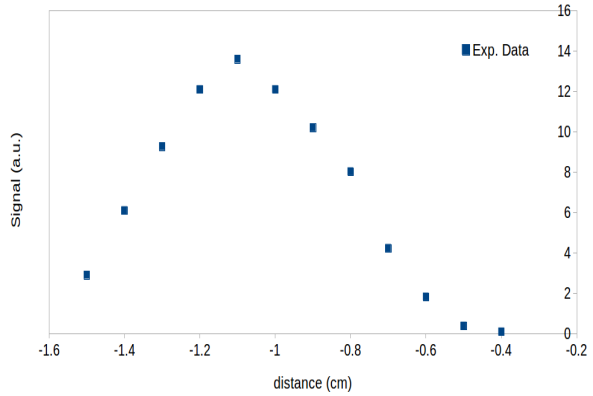

(e) distance: 5.5 cm

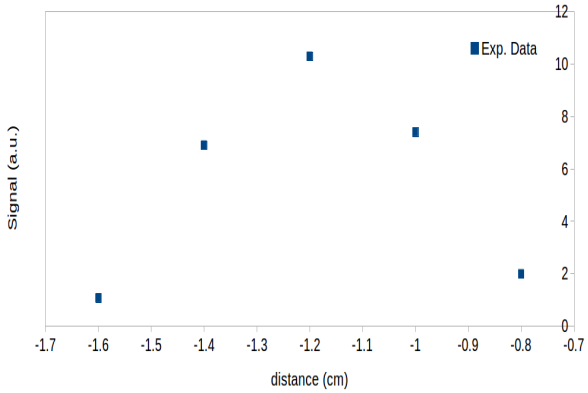

(f) distance: 6.5 cm

Figure 3.8: Proton beam lateral profile of the beam measured with the 1 mm fiber. Raw data.

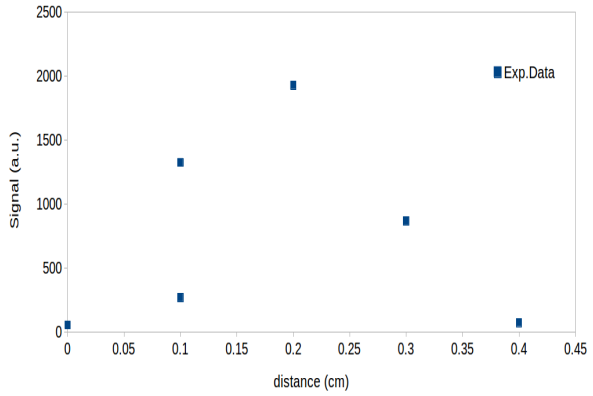

(a) distance:1.5 cm

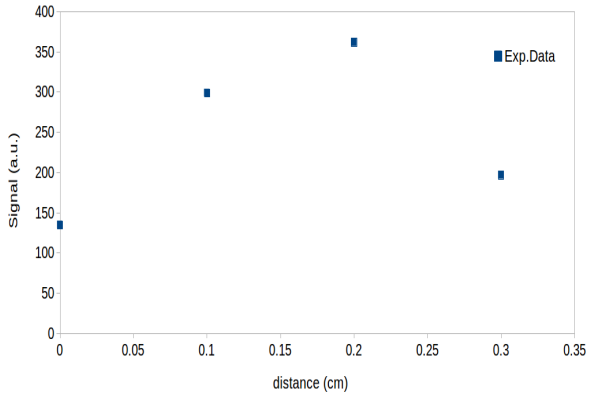

(b) distance: 2.5 cm

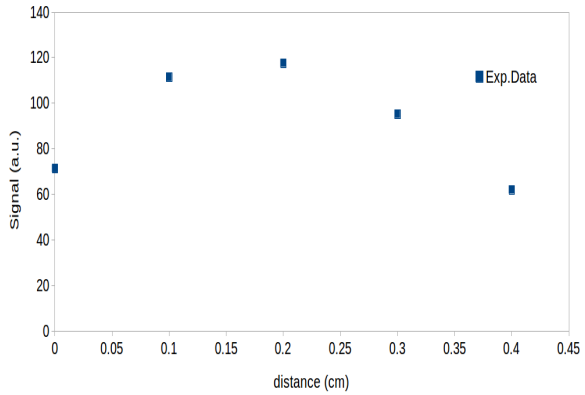

(c) distance: 3.5 cm

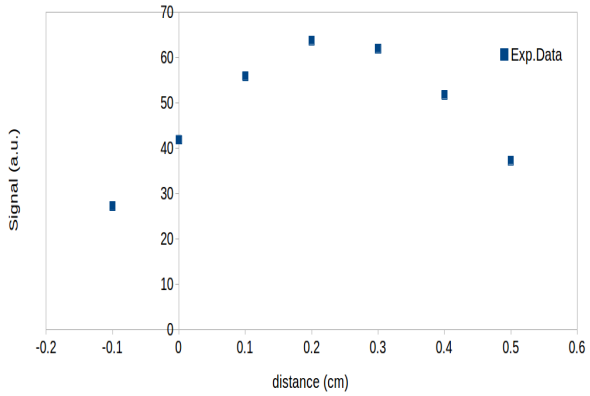

(d) distance: 4.5 cm

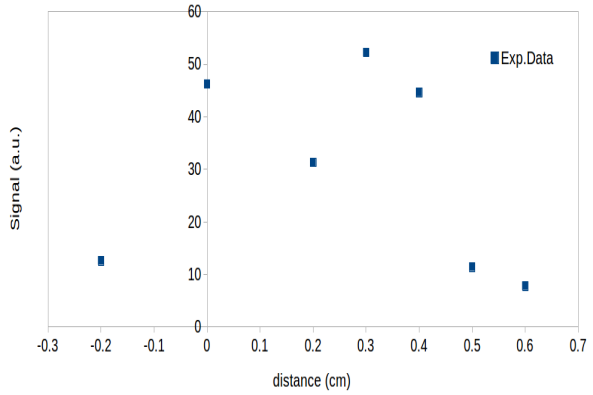

(e) distance: 5.5 cm

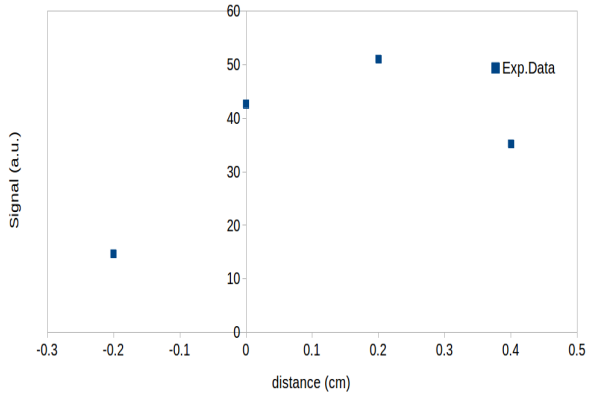

(f) distance: 6.5 cm

Figure 3.9: Proton beam lateral profile of the beam measured with the 2 mm fiber. Raw data.

This lateral scanning also allowed to measure if there was a disalignment in the irradiation box positioning. Figure 3.10 shows the lateral position of the points were the most signal was read and demonstrates that there is a disalignment in the irradiation box.The displacement shown in figure 3.10 equals to 9 degrees.

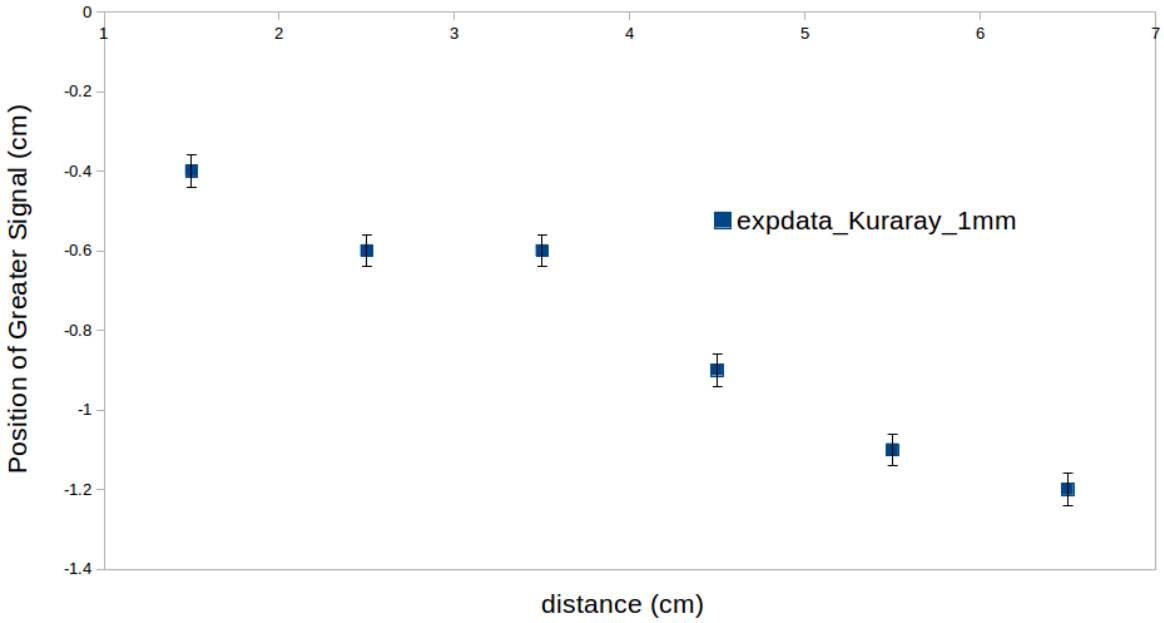

Figure 3.10: The position were the most signal was read. The points correspond to the position with most signal. The error bars correspond to the stepper motor resolution.

The fits showed that a Gaussian fit fits the data. The Full Width Half Maximum (FWHM) was taken as the beam's width for a certain position. This was used to measure the security distance between the phantom and the beam's exit (to avoid to puncture the the silver window) and was also used to introduce in the simulations the σ relative to the beam's Gaussian geometry, using the relation $FWHM = 2.355\sigma$.

Figure 3.11 is an example of a fit performed. The fitting software used is Fityk version 1.3.1.. This fit is performed with the Nelder-Mead Algorithm. The Nelder-Mead is a method that uses a simplex to find a local minimum of a function of several variables. For two variables, a simplex is a triangle, and the method is a pattern search that compares function values at the three vertices of the triangle. The worst vertex, where $f(x, y)$ is largest, is rejected and replaced with a new vertex. A new triangle is formed and the search is continued. The process generates a sequence of triangles (wich might have diferente shapes), for wich the function values at the vertices get smaller and smaller. The size of the triangles is reduced and the coordinates of the minimum point are found [41] [42].

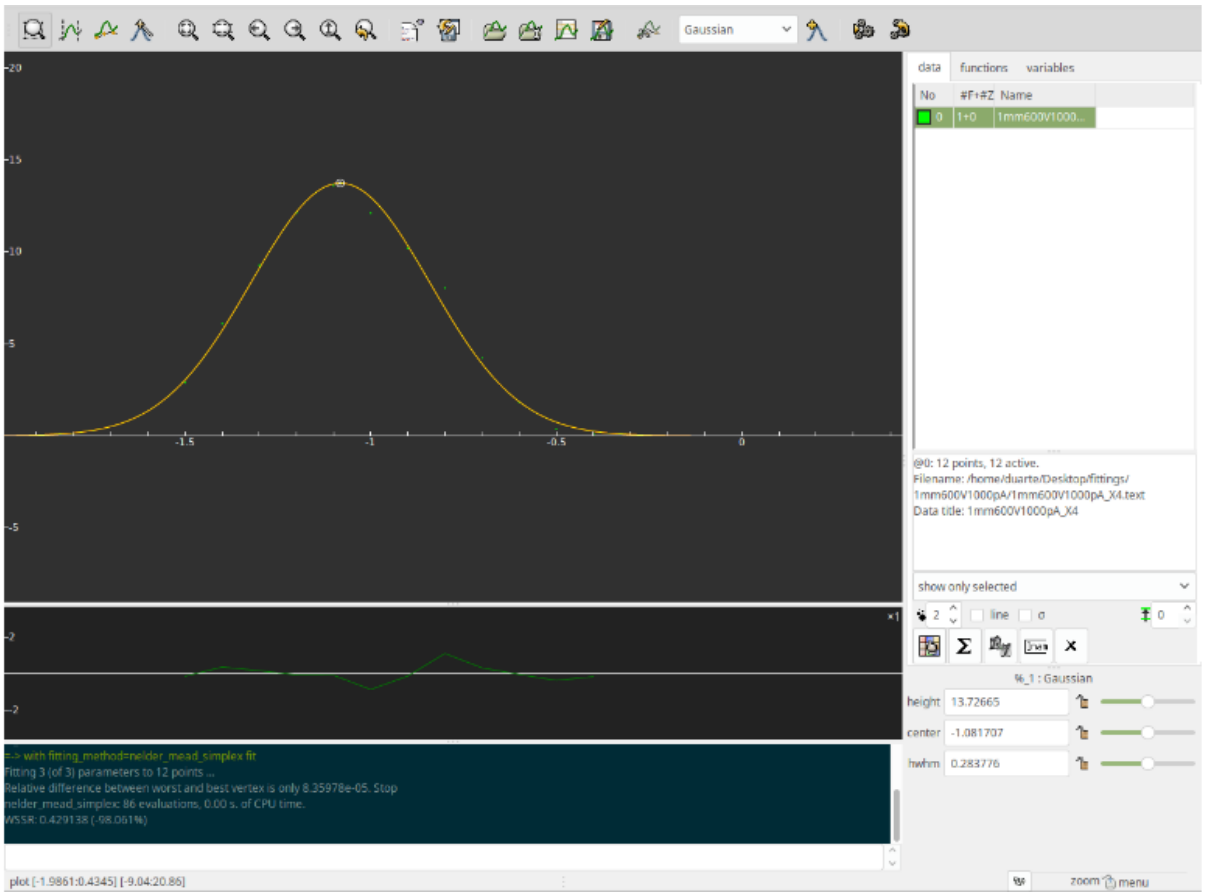

Figure 3.11: Screenshot of the fits of experimental data performed with the Fityk software.

Figure 3.12 shows the linear regression done with the width of the beam, for certain distances, measured with the 1 mm optical fiber.

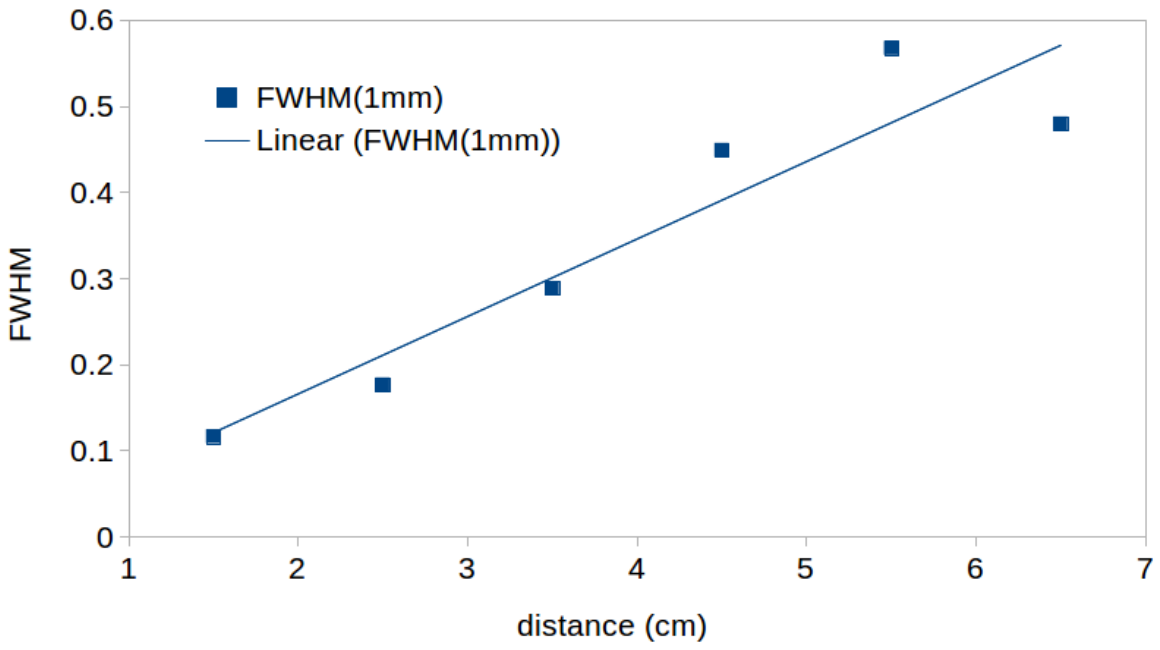

Figure 3.12: Linear regression made with the FWHM calculated with the Fityk software for the data measured with the 2 mm optical fiber.

Figure 3.13 shows the linear regression done with the width of the beam, for certain distances, measured with the 2 mm optical fiber.

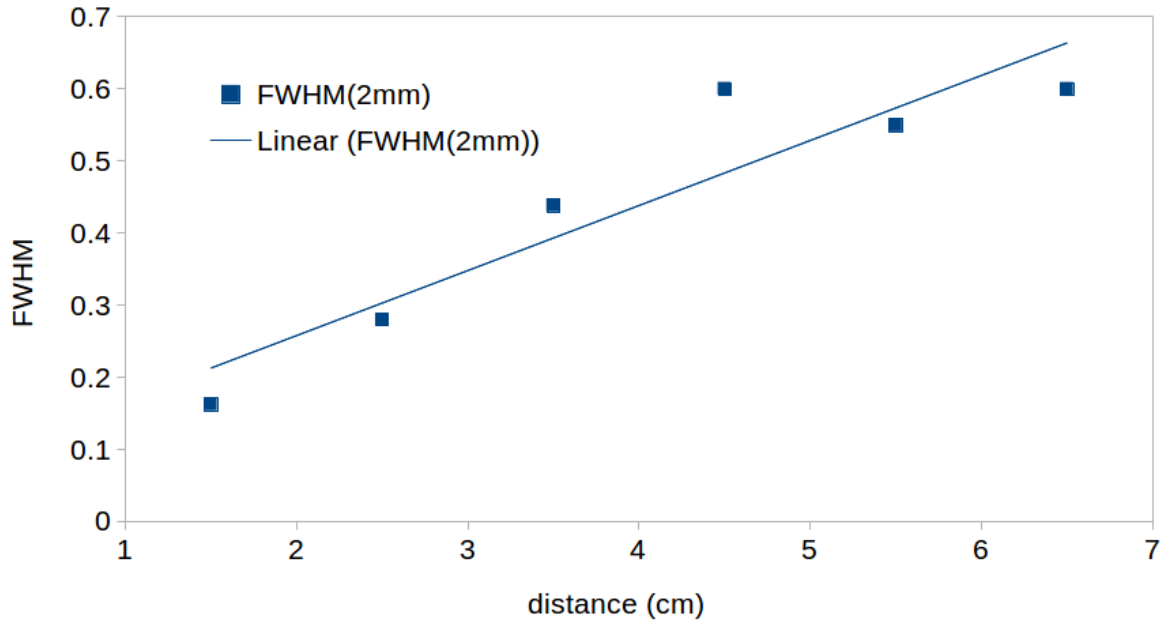

Figure 3.13: Linear regression made with the FWHM calculated with the Fityk software for the data measured with the 2 mm optical fiber.

With this linear regression's it is possible to make an estimate of the position of the accelerator's exit relative to the points considered as the optical fiber's position. The assumption made is that the position with FWHM equal to zero is the position of the accelerator's exit. To determine this position it is necessary to find the linear regression's zero. For the 1mm fiber it is the same as solving for x:

$$0.0899 \cdot x - 0.01349 = 0 \tag{3.2}$$

And for the 2mm fiber, again, it is necessary to solve for x:

$$0.0901 \cdot x + 0.0773 = 0 \tag{3.3}$$

This means that the we have:

- For the 1mm fiber, the position corresponding to the accelerator´s exit, is: 0.15 cm.
- For the 2mm fiber, the position corresponding to the accelerator's exit, is: - 0.85 cm.

It is important to refer that these numbers don't need to coincide. When there is a switch from one fiber to the other the setup is reassembled and so the phantom position can change, the fiber's position inside the phantom can change and it all contributes to get a different security distance value. But these positions are all within the expected range.

Figure 3.14 and figure 3.15 show the lateral profile of the beam, measured with a 1mm and a 2mm optical fiber, compared with the simulations performed with pMC.

This simulation was performed with a gaussian beam defined by:

$$\sigma_x = 0.0125 \cdot z_{det} \tag{3.4}$$

$$\sigma_y = 0.0125 \cdot z_{det} \tag{3.5}$$

$$x = x_{src} + xrand \cdot \sigma_x \tag{3.6}$$

$$y = y_{src} + yrand \cdot \sigma_y \tag{3.7}$$

$$r = \sqrt{x^2 + y^2 + z_{det}^2} \tag{3.8}$$

$$u = \frac{x}{r} \tag{3.9}$$

$$v = \frac{y}{r} \tag{3.10}$$

$$w = \frac{z_{det}}{r} \tag{3.11}$$

where σ_x (σ_y) is the standard deviation for the x-axis distribution (y-axis distribution), this value of 0.0125 was found by starting with $FWHM \cdot 2.355$ for each position, but searching for a formula that depended on the position of the fiber, this was achieved solving $FWHM \cdot 2.355 = \chi \cdot z_{det}$ for χ and making the mean of this value for several positions the value of $\chi = 0.0125$ was reached; x (y) is the position of the particle in the respective axis defined by x_{src} (y_{src}) each is the position of the source in the x (y) axis, defined, also, by xrand (yrand) that corresponds to a random number generator that follows a gaussian distibution with median value equal to 0 and standard deviation equal to 1; r from the source to the particles position and u, v, w are the director vectors that define the particle's trajectory.

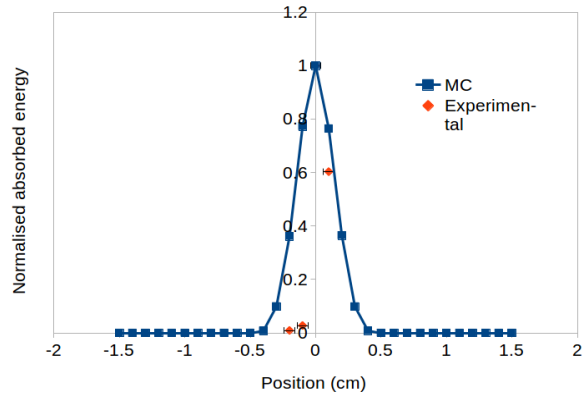

(a) distance:1.5 cm

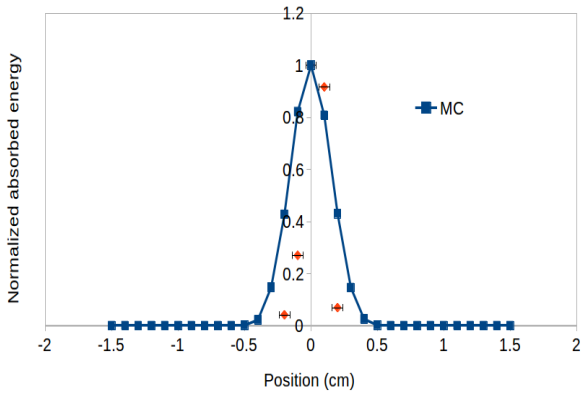

(b) distance: 2.5 cm

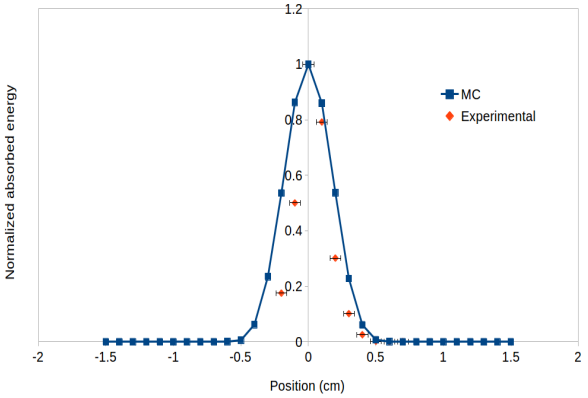

(c) distance: 3.5 cm

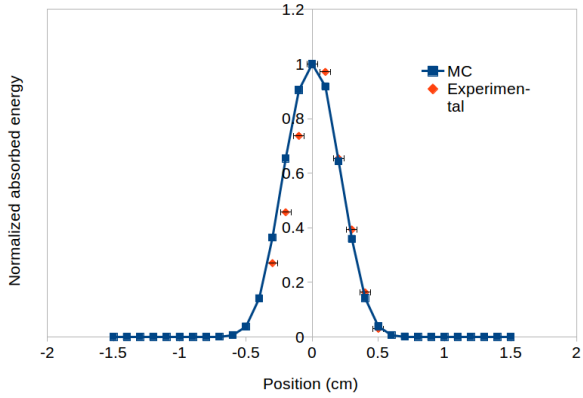

(d) distance: 4.5 cm

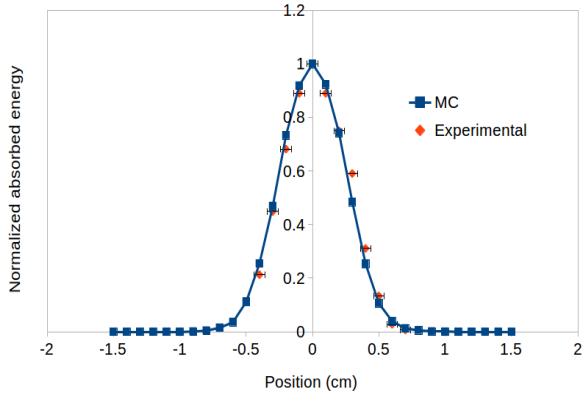

(e) distance: 5.5 cm

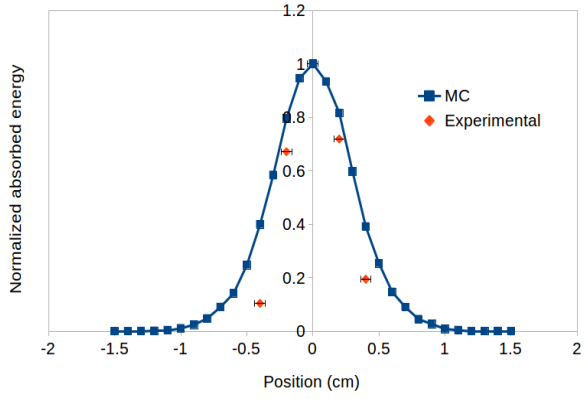

(f) distance: 6.5 cm

Figure 3.14: Proton beam lateral profile of the beam measured with the 1mm fiber. Simulations performed with pMC. The error bars represent the stepper motor used.

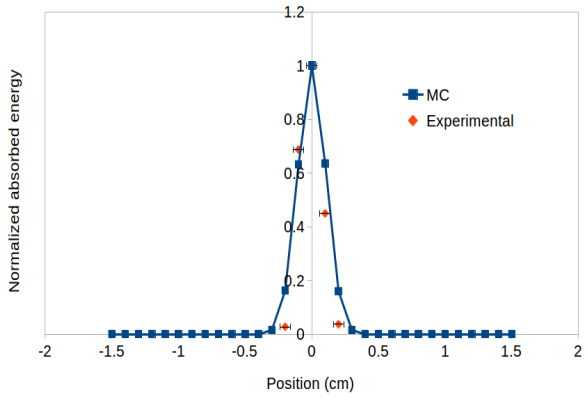

(a) distance: 1.5 cm

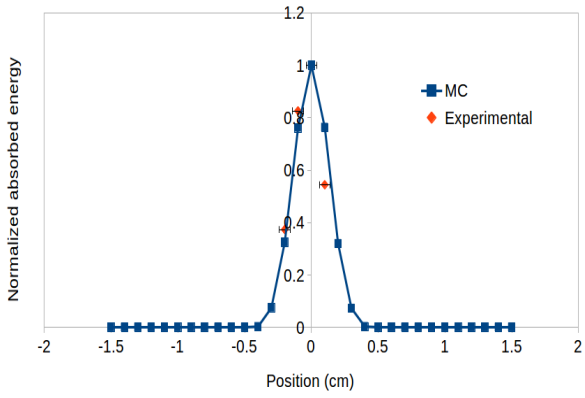

(b) distance: 2.5 cm

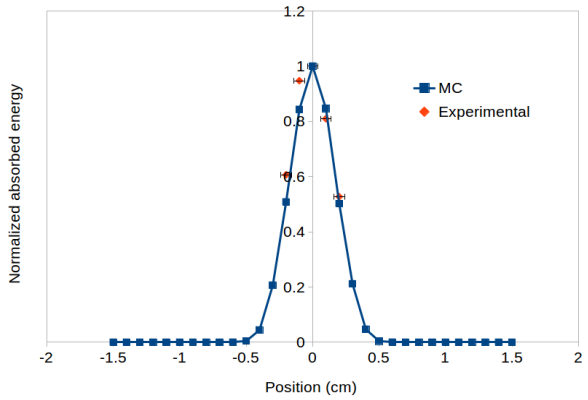

(c) distance: 3.5 cm

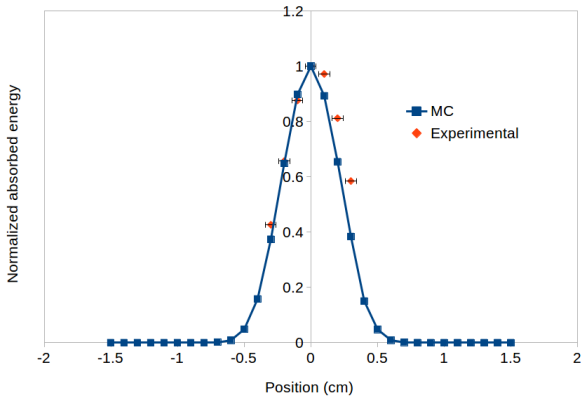

(d) distance: 4.5 cm

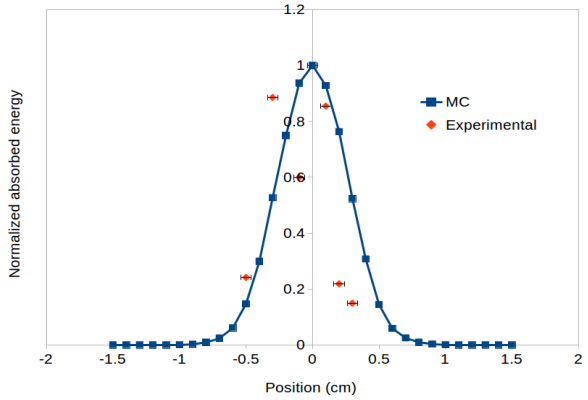

(e) distance: 5.5 cm

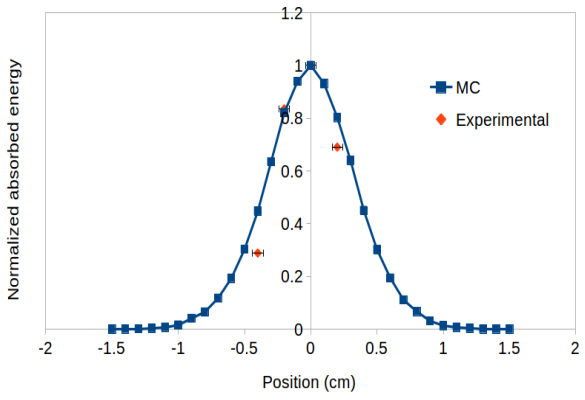

(f) distance: 6.5 cm

Figure 3.15: Proton beam lateral profile of the beam measured with the 2mm fiber. Simulations performed with pMC.The error bars represent the stepper motor used.

The figures show that the simulations can be compared to the experimental results and that a Gaussian geometry replicates really well the CTN's beam's geometry.

3.3.2 LONGITUDINAL MEASUREMENTS

Figure 3.16 shows the beam's longitudinal profile has it has measured by the 1mm SCSF-78 Kuraray optical fiber. The points that were considered for the graph are the lateral points that have the most signal.

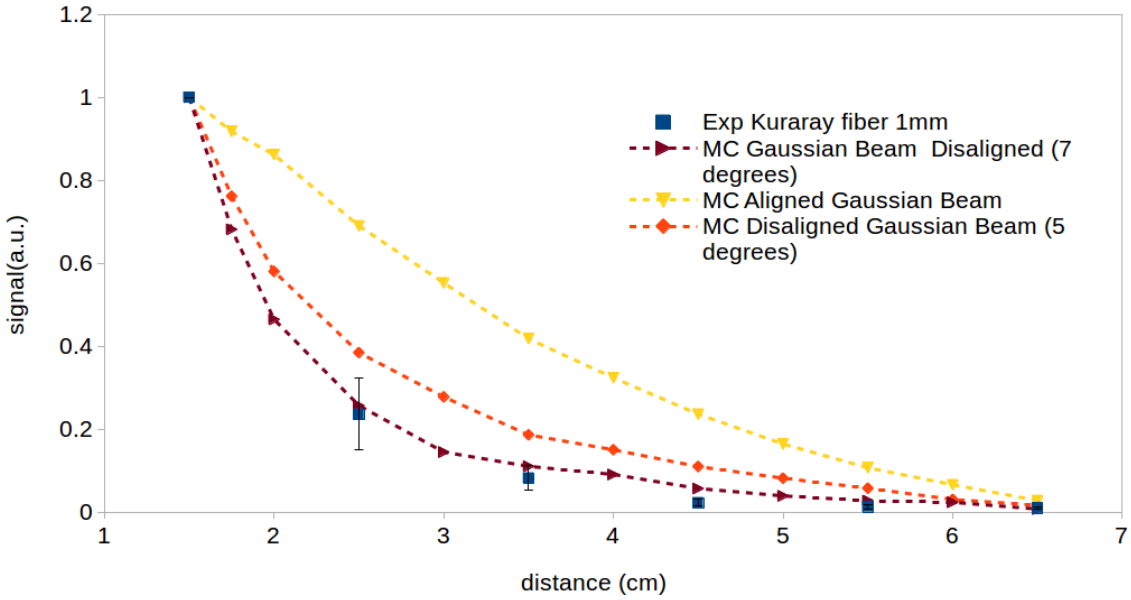

Figure 3.16: Energy deposition in the 1mm SCSF-78 Kuraray optical fiber, compared with a pMC simulation with a fiber deviation of 5 degrees and 7 degrees with a Gaussian beam and a perfectly aligned fiber also with a Gaussian beam.

It was also tried to performed simulations that consider a variable beam energy. This was made considering first the beam's energy between 1.8 MeV and 2.2 MeV and then between 1.8 MeV and 2 MeV, as can be seen in figure 3.17. The variable energy was achieved with, for example: $1.8 + 0.4 \cdot rand()$ where rand() is an uniform random number generator between 0 and 1.

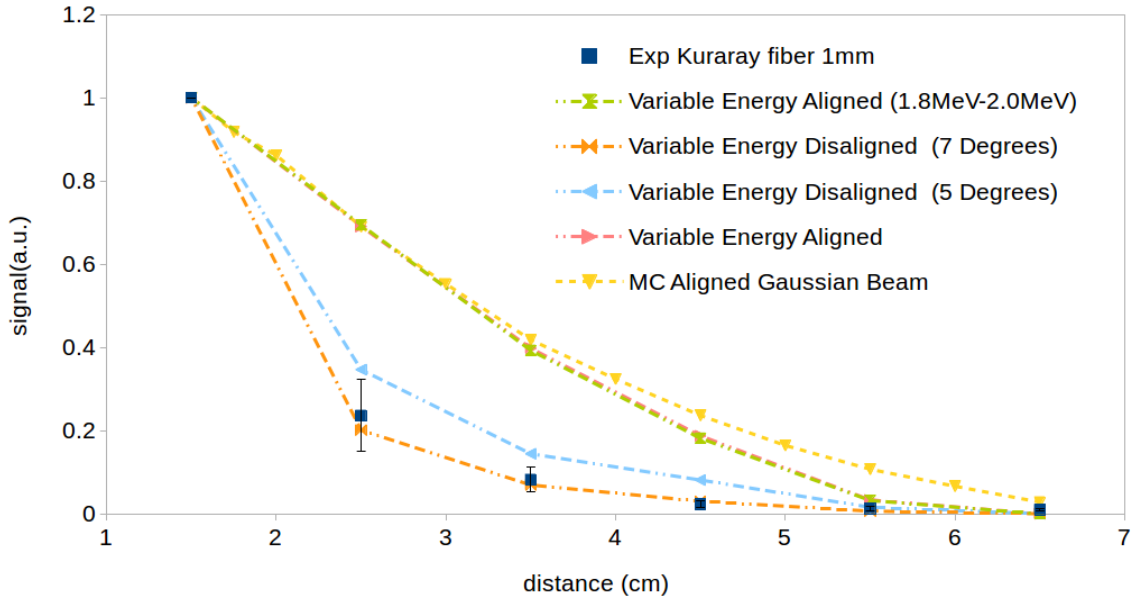

Figure 3.17: Energy deposition in the 1mm SCSF-78 Kuraray optical fiber, compared with a pMC simulation with a fiber deviation of 5 degrees and 7 degrees with a Gaussian beam with energy between 1.8 MeV and 2.2 MeV, an aligned beam with energy between 1.8 MeV and 2.2 MeV, an aligned beam with energy between 1.8 and 2 MeV and perfectly aligned fiber with a Gaussian beam with no variable energy.

With this variablility in the energy it was expected that a smaller angle of displacement was needed to explain the experimental measurements. But as can be seen in figure 3.17 it doesn't translate into a significant variation.

Figure 3.18 shows the beam's longitudinal profile has it has measured by the 2 mm BCF-12 SaintGoban optical fiber. The same point selection method was applied.

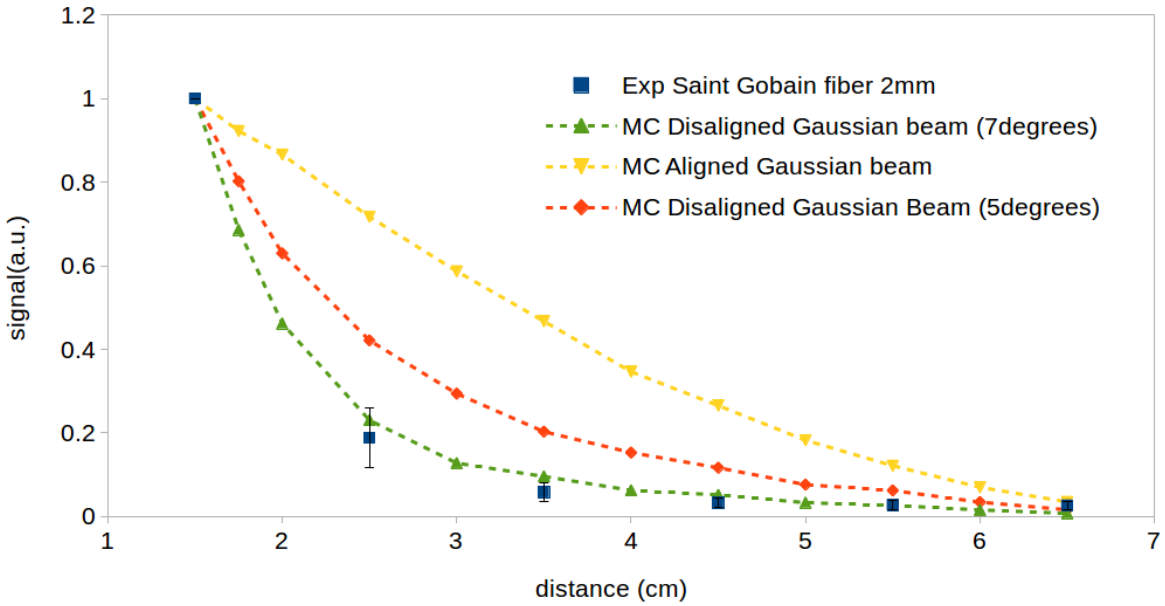

Figure 3.18: Energy deposition in the 2mm BCF-12 StainGoban optical fiber, compared with a pMC simulation with a fiber deviation of 5 degrees and a Gaussian beam and a perfectly aligned fiber also with a Gaussian beam.

The second set of points confirmed the first set of measurements. So, the fact that a Bragg Peak is not visible cannot be entirely due to the fact that the positioning system wasn't good enough and to the fact that the optical fiber wasn't perfectly aligned.The best explanation found considers three phenomena:

- The fact that the beam only has 2 MeV. This is important because a 2 MeV proton can't travel from one way of the fiber to the other, in other words, the range of a 2 MeV proton in PMMA is smaller than the fiber's diameter. This means that the majority of the proton's that interact with the fiber will deposit their entire energy on the fiber, and because of that what is being measured by the fiber is not the energy deposited by the proton's in a dx the size of the fiber, but is actually measuring the protons energy.
- When a narrow beam is used the intensity will rapidly decrease with distance, so when the fiber is close to the beam's exit it will interact with a lot of protons, but when the fiber is far from the beam's exit it will not interact with nearly as much protons as before and that accounts to a huge discrepancy in the signal read. As can be seen in figures 3.19 and 3.20
- Figures 3.18 and 3.16 show that the best prediction includes the Gaussian beam and a displacement of 7 degrees. This displacement can have it's origin in imperfections in the alignment of the base used for the positioning system, in the fact that the stepper motors don't have enough resolution or in the fact that the box wasn't correctly placed in the positioning system, wich is shown in figure 3.10.

It is proven, by simulation, that the number of protons that touch the fiber decreases over the longitudinal axis can be seen in figure 3.19 and figure 3.20. This decrease in the number of protons that interact with the optical fiber doesn't follow a $\frac{1}{r^2}$ because the simulation was made with a beam that spreads in a Gaussian way and not in an isotropic way.

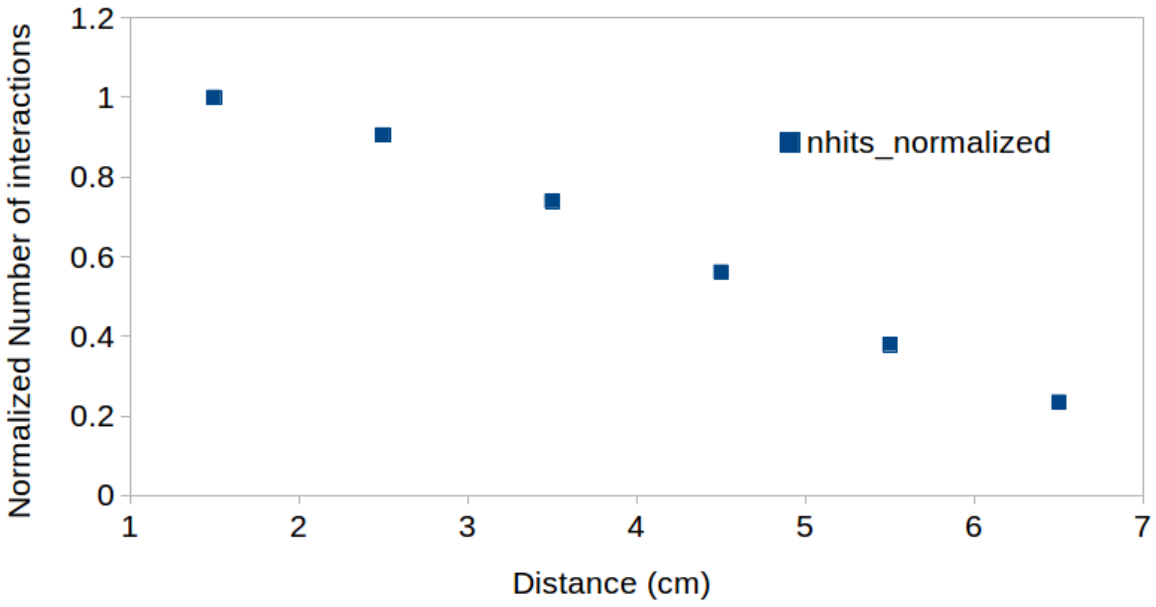

Figure 3.19: The points represent the normalized number of protons that interacted with a 2 mm optical fiber. The points choosen are the lateral points with the greatest number of counts.

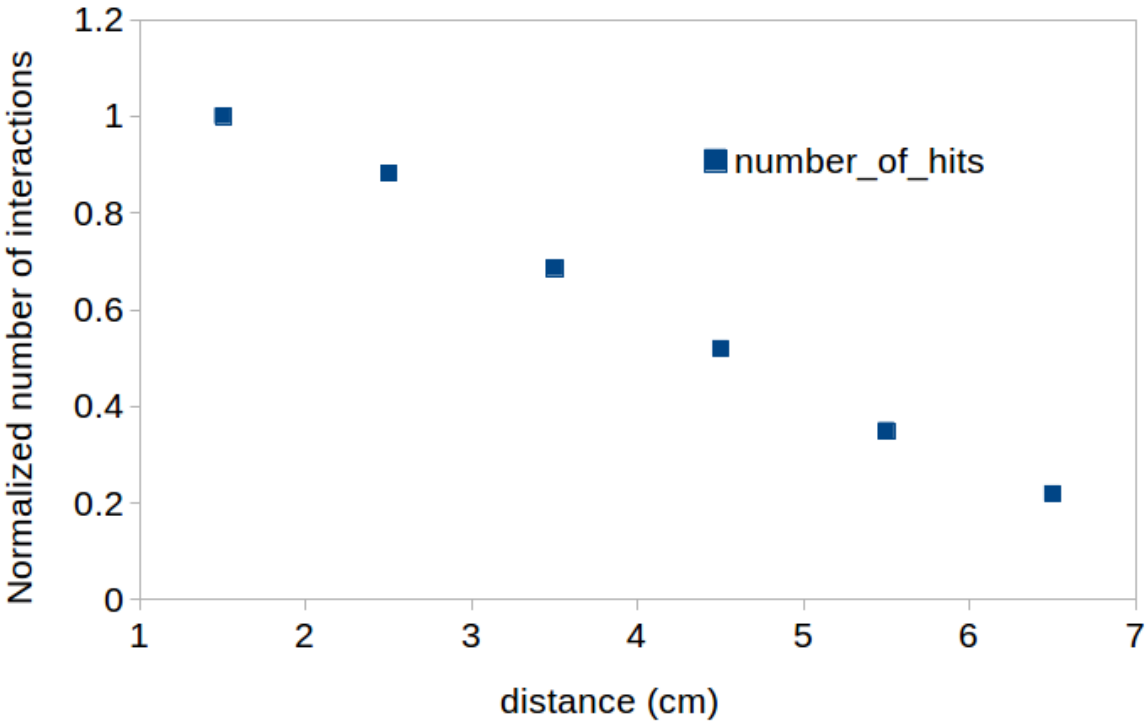

Figure 3.20: The points represent the normalized number of protons that interacted with a 1 mm optical fiber. The points choosen are the lateral points with the greatest number of counts.

The data collected during the measurements doesn't allow for the extraction of the Birk's coefficient(s) for the fibers used.

4 CONCLUSION

The objective of this work was to develop a experimental setup to map the Bragg Peak of proton beams of different energies and to study the response of the scintillator's used. The setup was developed and consists of: an irradiation chamber to prevent the reading of room light from spoiling the measurements; a positioning system that allows the user to place with precision the optical fiber and the optical fibers chosen to perform the measurements.

This work represents the start of a period of research in proton therapy dosimetry in the LIP's Medical Physics group. The ground work to perform the measurements of proton beam's energy deposition with optical fibers is set. Furthermore, and most importantly, a methodology was created.

There certain improvements to be made in the setup developed:

- The irradiation box has to be improved so that it becomes more user friendly, particularly in what has to do with the insertion of the optical fiber inside it.
- The positioning system shows some fragilities that need to be addressed, specifically with the motors and the timing belt. So, in the future it is important to perform a better rehabilitation of the positioning system, maybe buying a new set of motors that offer a higher amount of torque and that enables the positioning system to travel farther would solve the problem. Besides that, the driver bought showed to be a very good fit and easy to use.
- The software pMC was very useful during this work and it presents good predictions, although it presents some differences when compared to FLUKA. In the future it would interesting to develop a GUI to be able to visualize the simulations geometry since the geometry is a great source of bugs.
- The alignment of the irradiation box has to be improved, as well as the alignment of the beam.

During the work it wasn't possible to achieve all the desired goals, because as stated in chapter 3 the quality of the data used isn't good enough so that we can extract the Birk's coefficients for the fibers used. Hopefully it will be possible to perform the analysis of the Birk's coefficients in a more stable beam were it is possible to know the beam's intensity, that is why using the ICNAS's cyclotron is of great interest. The biggest fragility in this work is the fact that it is impossible to control the beam's intensity.

There is little work done in low energy proton dosimetry. This work showed that it is difficult to map the Bragg Peak with a low energy and with a source with low width.

REFERENCES

[1] Sam Beddar and Luc Beaulieu. *Scintillation Dosimetry*, volume 1. 2016.

[2] D.W. Krekelberg W.P. Shen V. K., Siderius and Eds. Hatch, H.W. NIST Standard Reference Simulation Website, NIST Standard Reference Database Number 173. *National Institute of Standards and Technology*, 2017.

[3] S-O Flyckt and Carole Marmonier. PHOTOMULTIPLIER TUBES principles & applications. Technical report, 2002.

[4] Arrick Robotics - Stepper motor, Positioning, Automation, Mobile Robots, Resources. *https://www.arrickrobotics.com/index.html*, October, 2019.

[5] Adafruit Industries, Unique & fun DIY electronics and kits. *https://www.adafruit.com/October, 2019.*

[6] Raspberry Pi—Teach. learn, and make with Raspberry Pi. https://www.raspberrypi.org/*, October, 2019.*

[7] Jeffrey Tobias and Daniel Hochhauser. Cancer and its Management: Sixth Edition*. Wiley-Blackwell, Oxford, UK, 12 2009.*

[8] Miodrag Gužvić and Christoph A. Klein. The Biology of Cancer Metastasis. pages 117–128. 2009.

[9] Martyn Plummer, Catherine de Martel, Jerome Vignat, Jacques Ferlay, Freddie Bray, and Silvia Franceschi. Global burden of cancers attributable to infections in 2012: a synthetic analysis. The Lancet Global Health*, 4(9):e609–e616, 9 2016.*

[10] Ahmedin Jemal, R. Siegel, E. Ward, T. Murray, J. Xu, and M. J. Thun. Cancer Statistics, 2007. CA: A Cancer Journal for Clinicians*, 57(1):43–66, 1 2007.*

[11] J. Ferlay, M. Colombet, I. Soerjomataram, T. Dyba, G. Randi, M. Bettio, A. Gavin, O. Visser, and F. Bray. Cancer incidence and mortality patterns in Europe: Estimates for 40 countries and 25 major cancers in 2018. European Journal of Cancer*, 103:356–387, 11 2018.*

[12] David A Jaffray and Mary K Gospodarowicz. Radiation Therapy for Cancer. In Disease Control Priorities, Third Edition (Volume 3): Cancer*, pages 239–247. The International Bank for Reconstruction and Development / The World Bank, 11 2015.*

[13] BS Rao. Handbook of radiobiology. Journal of Medical Physics*, 42(3):194, 2017.*

[14] Wayne D Newhauser, Amy Berrington de Gonzalez, Reinhard Schulte, and Choonsik Lee. A Review of Radiotherapy-Induced Late Effects Research after Advanced Technology Treatments. Frontiers in Oncology*, 6:13, 2016.*

[15] Harald Paganetti. Proton Therapy Physics(Series in Medical Physics and Biomedical Engineering)*. 2012.*

[16] Adrie J.J. Bos. Fundamentals of radiation dosimetry. In AIP Conference Proceedings*, volume 1345, pages 5–23, 2011.*

[17] A. H.W. Nias. Handbook of radiobiology. International Journal of Radiation Biology*, 47(4):476–477, 4 1985.*

[18] 3rd International Conference on Dosimetry and its Applications (ICDA-3): Home.

[19] Frank Herbert Attix. Introduction to Radiological Physics and Radiation Dosimetry*. Wiley, 11 1986.*

*[20] Nobuko Takahashi, Masahito Tomizawa, and Jinzo Kobayashi. Optical Activity and Electrogyration Effect of Co 3 B 7 O 13 I and Cu 3 B 7 O 13 Cl *.* Japanese Journal of Applied Physics*, 31(Part 1, No. 9B):3209–3211, 2005.*

[21] Glenn F. Knoll and H. W. Kraner. Radiation Detection and Measurement*, volume 69. 1981.*

[22] Klaus D. Hildenbrand. Scintillation detectors. In Experimental Techniques in Nuclear Physics*, pages 59–86. Springer Berlin Heidelberg, Berlin, Heidelberg, 2011.*

[23] J. W. Blue and D. C. Liu. Scintillation Response of Aikali Iodides to Alpeha Particles and Protons. IRE Transactions on Nuclear Science*, 9(3):48–51, 6 1962.*

[24] R. Gwin and R. B. Murray. Scintillation Process in CsI(Tl). I. Comparison with Activator Saturation Model. Physical Review*, 131(2):501–508, 7 1963.*

[25] Kuraray Co. Ltd. Plastic Scintillating Fibers. Data Sheet, https://www.kuraray.com/products/category/fiber*, October, 2019.*

[26] O. Borshchev, A. B.R. Cavalcante, L. Gavardi, L. Gruber, C. Joram, S. Ponomarenko, O. Shinji, and N. Surin. Development of a New Class of Scintillating Fibres with Very Short Decay Time and High Light Yield. Journal of Instrumentation*, 12(5):P05013–P05013, 5 2017.*

[27] SaintGoban Co. Ltd. Plastic Scintillating Fibers. Data Sheet, https://www.crystals.saint-gobain.com/sites/imdf.crystals.com/files/documents/fiber-product-sheet.pdf*, October, 2019.*

[28] S Buranurak and C E Andersen. Fiber optically coupled radioluminescence detectors: A short review of key strengths and weaknesses of BCF-60 and Al2O3:C scintillating-material based systems in radiotherapy dosimetry applications. In Journal of Physics: Conference Series*, volume 860, page 012028, 6 2017.*

[29] Mortimer Abramowitz and Michael Davidson. Concepts in Digital Imaging Technology: Photomultiplier Tubes, 2016.

[30] Home — LibreOffice - Free Office Suite, https://www.libreoffice.org/. October, 2019.

[31] M. A. Farouk, M. H. Nassef, A. Z. El-Behay, and I. I. Zaloubovsky. Measurement of the thickness of thin foils. Nuclear Instruments and Methods*, 35(2):210–212, 1965.*

[32] NIH. Benzene;4,5-dibromo-2H-thiophen-2-ide;platinum(2+);2-pyridin-2-ylpyridine — C20H14Br2N2PtS - PubChem, 2019.

[33] José Lopes, Francisco Alegria, Luís Redondo, Jorge Rocha, and Eduardo Alves. Computer Control of a 3 MV Van de Graaff Accelerator. Metrology and Measurement Systems*, 17(3):415–425, 1 2010.*

[34] Edmund Wilson. An Introduction to Particle Accelerators*. Oxford University Press, 2010.*

[35] Art B. Owen. Monte Carlo theory, methods and examples*. 2013.*

[36] Kenneth Wood, Barbara Whitney, Jon Bjorkman, and Michael Wolff. Introduction to Monte Carlo Radiation Transfer. Technical report.

[37] Tao Pang, Harvey Gould, and Jan Tobochnik. An Introduction to Computational Physics *, volume 67. 2002.*

[38] Giuseppe Battistoni, Julia Bauer, Till T. Boehlen, Francesco Cerutti, Mary P. W. Chin, Ricardo Dos Santos Augusto, Alfredo Ferrari, Pablo G. Ortega, Wioletta Kozłowska, Giuseppe Magro, Andrea Mairani, Katia Parodi, Paola R. Sala, Philippe Schoofs, Thomas Tessonnier, and Vasilis Vlachoudis. The FLUKA Code: An Accurate Simulation Tool for Particle Therapy. Frontiers in Oncology*, 6(May), 2016.*

[39] Luis Peralta and Alina Louro. AlfaMC: A fast alpha particle transport Monte Carlo code. Nuclear Instruments and Methods in Physics Research, Section A: Accelerators, Spectrometers, Detectors and Associated Equipment*, 737:163–169, 2 2014.*

[40] James F. Ziegler, M.D. Ziegler, and J.P. Biersack. SRIM – The stopping and range of ions in matter (2010). Nuclear Instruments and Methods in Physics Research Section B: Beam Interactions with Materials and Atoms*, 268(11-12):1818–1823, 6 2010.*

[41] Alberto Moraglio and Colin G. Johnson. Geometric generalization of the nelder-mead algorithm. In Lecture Notes in Computer Science (including subseries Lecture Notes in Artificial Intelligence and Lecture Notes in Bioinformatics)*, volume 6022 LNCS, pages 190–201. Springer, Berlin, Heidelberg, 2010.*

[42] J. H. Mathews and K. K. Fink. Nelder-Mead method. In Numerical Methods Using Matlab*, pages 430–437. 2004.*